

Masses, Radii, and Equation of State of Neutron Stars

Feryal Özel¹ and Paulo Freire²

¹Department of Astronomy, University of Arizona, Tucson, AZ 85721, USA;
email: fozel@email.arizona.edu

²Max-Planck-Institut für Radioastronomie, Auf dem Hügel 69, D-53121, Bonn, Germany; email: pfreire@mpifr-bonn.mpg.de

Xxxx. Xxx. Xxx. Xxx. YYYY. 00:1–39

This article's doi:
10.1146/((please add article doi))

Copyright © YYYY by Annual Reviews.
All rights reserved

Keywords

neutron stars, dense matter, pulsars, pulsar timing, X-ray sources

Abstract

We summarize our current knowledge of neutron star masses and radii. Recent instrumentation and computational advances have resulted in a rapid increase in the discovery rate and precise timing of radio pulsars in binaries in the last few years, leading to a large number of mass measurements. These discoveries show that the neutron star mass distribution is much wider than previously thought, with 3 known pulsars now firmly in the $1.9\text{--}2.0\ M_{\odot}$ mass range. For radii, large, high quality datasets from X-ray satellites as well as significant progress in theoretical modeling led to considerable progress in the measurements, placing them in the $9.9\text{--}11.2\text{ km}$ range and shrinking their uncertainties due to a better understanding of the sources of systematic errors. The combination of the massive neutron star discoveries, the tighter radius measurements, and improved laboratory constraints of the properties of dense matter has already made a substantial impact on our understanding of the composition and bulk properties of cold nuclear matter at densities higher than that of the atomic nucleus, a major unsolved problem in modern physics.

1. INTRODUCTION

Our understanding of neutron stars has changed drastically since the Annual Reviews article of Wheeler (1966), when not a single neutron star was known and the discussion consisted of an entirely theoretical treatment of collapsed dense stars. The change has been most rapid in the last decade, when the discovery and precise timing observations of pulsars has proceeded at an ever accelerating rate, the new generation X-ray and γ -ray telescopes have provided high quality, large datasets, and a large body of theoretical work on neutron star emission properties and spacetimes have enabled significant recent developments in our ability to model these extreme objects and interpret the observations in solid frameworks.

We now know precise masses for ~ 35 neutron stars spanning the range from 1.17 to $2.0 M_{\odot}$ and can pin down the radii of more than a dozen to the 9.9 – 11.2 km range. The combination of the heaviest known neutron star mass with the existing radius measurements already places significant constraints on the cold dense matter equation of state up to densities that are 8 times the nuclear density.

Certain characteristics of neutron stars have been known for a while. Shortly after the discovery of pulsars (Hewish et al. 1968), it became apparent that they are the observational manifestation of extremely compact stars made primarily of neutrons. It was also evident that, while the neutron degeneracy pressure played a role in supporting these compact objects against gravitational collapse, it was not sufficient to hold up a star beyond $0.7 M_{\odot}$ (Oppenheimer & Volkoff 1939; Tolman 1939), and that repulsive nuclear forces were necessary in shaping their structure (Harrison et al. 1965). Earlier calculations of the interiors treated nucleons with approximate potentials and predicted masses in the $0.5 - 3 M_{\odot}$ range and radii between 7 and 20 km. Stars of such extreme compactness have central densities that are 5-10 times the nuclear saturation density $\rho_{\text{sat}} = 2.8 \times 10^{14} \text{ g cm}^{-3}$.

While the nuclear models improved over the years, the major advances have come from astrophysical observations and models because terrestrial experiments do not approach densities similar to that of neutron star cores (see section 4.2). Theoretical work is guided by the well developed effective field theory approaches and the rapidly developing QCD calculations but there remain very large uncertainties in our understanding of the actual compositions of the cores. Open questions include the composition of matter at high densities, such as the density at which matter needs to be described by quarks and no longer by nucleons, as well as the presence of strangeness or boson condensates in such matter; the isospin symmetry energy that defines the energy difference between normal and neutron-rich matter and, ultimately, the ability to calculate matter in β -equilibrium from first principles; and the role and reliability of calculations of n-body interactions. Despite the large number of possibilities, each theoretical model, or its resulting equation of state, can be mapped into a mass-radius relation by solving the general relativistic structure equations. This, in turn, allows measurements of the neutron star masses and radii to place strong constraints on the properties and interactions of cold, ultradense matter, as we will discuss in this review. These same observations also provide excellent tests of general relativity in the strong-field regime, using pulsars as well as neutron star surfaces as testbeds.

The recent series of investigations of neutron star masses and radii are motivated not only by the aim of probing physics in new regimes, but also because of the forefront role neutron stars play in many astrophysical phenomena. Neutron stars are associated with numerous explosive, transient, and non-electromagnetic events, and neutron star properties play a role in shaping each one of them. The primary sources of gravitational waves that are expected to be detected with the gravitational wave detector Advanced LIGO are the neutron star-neutron star and neutron star-black hole mergers. These systems are also thought to be the central engines of short gamma-ray bursts (see Nakar 2007 for a review). The dynamics of the mergers, the gravitational waveforms in late stages of coalescence, the lifetime of merger disks and the resulting black

hole formation timescales, as well as any accompanying bursts of neutrino, gamma-ray, and/or optical emission depends sensitively on the neutron-star mass, radius, and the equation of state (Baiotti, Giacomazzo & Rezzolla 2008; Metzger et al. 2010; Hotokezaka et al. 2011; Bauswein et al. 2012; Lackey et al. 2012; Kumar & Zhang 2015).

From a stellar lifecycle and source population point of view, studies of neutron stars prove to be equally important. Different equations of state allow different maximum masses for neutron stars and, thus, determine the dividing line between neutron stars and black holes. This has a direct impact on the outcomes of supernova explosions and the nature of compact remnants, as well as on the numbers of neutron stars and black holes in the Galaxy. This, in turn, affects the number of observable compact object binaries, their properties, and possible merger/gravitational-wave event rates. In fact, the supernova mechanism itself is affected by the equation of state of ultradense matter. The hot dense matter EoS, an extension of the cold one probed by neutron stars, determines explosion conditions (e.g., Janka et al. 2007) and is crucial for understanding core collapse supernova explosions and the associated phenomena including mass loss, r-process nucleosynthesis, gravitational wave and neutrino emission.

The tremendous advance in the measurements of neutron star masses, radii, and the dense matter equation of state have come from a diverse array of techniques, applied to many different populations of neutron stars, and enabled by observations in all wavelengths from the radio to gamma rays. For example, while the precise mass measurements have largely resulted from radio observations of pulsars, the radius measurements have been almost exclusively been a result of X-ray observations of neutron stars in low-mass X-ray binaries. In this review, we will focus on the latest mass and radius measurements of neutron stars and their implications for the dense matter equation of state, as well as a number of questions that remain open.

2. NEUTRON STAR MASS MEASUREMENTS

The vast majority of the precise mass measurements of neutron stars have been performed using radio observations of rotation-powered pulsars. Currently more than 2500 pulsars are known in the Galaxy (Manchester et al. 2005), most of which are detectable as radio pulsars, but also some observed in X-rays and an increasingly large number detected in gamma rays¹ (Abdo et al. 2013; Caraveo 2014).

About 90% of radio pulsars are isolated. Their masses cannot be measured, since all of the current methods rely on precise tracking of the orbital motions through the arrival times of the observed pulsations. The remaining 250 pulsars are located in binary systems (three of these are in multiple component systems). We will now focus exclusively on these.

Most of the pulsars in binaries are “recycled”: at some point during the evolution of their companion there was mass transfer from the companion to the neutron star. The mass transfer can, in principle, increase the pulsar mass significantly, but its clearest effect is the spin-up of the pulsar (to spin frequencies as high as 716 Hz, see Hessels et al. 2006) and – by mechanisms that are poorly understood – a sharp reduction in the pulsar’s magnetic field, to values smaller than 10^{11} G. This process produces a wide variety of binary pulsars (for a recent review see, e.g., Lorimer 2008). Those of greatest interest to us are the systems where both components are compact: the double neutron star systems (DNSs) and the millisecond pulsar - white dwarf (MSP-WD) systems.

¹<https://confluence.slac.stanford.edu/display/GLAMCOG/Public+List+of+LAT-Detected+Gamma-Ray+Pulsars>

2.1. Timing binary pulsars

The extraordinary long-term rotational stability of recycled pulsars and their fast rotation makes them uniquely useful for timing. If a recycled pulsar is in a binary system (as it often happens), then we can use this precise timing to measure its orbital motion with astounding precision.

In Newtonian gravity, the part of the orbital motion we can observe (generally along the line of sight only) can be described by five Keplerian parameters: the binary period P_b , the orbital eccentricity e , the projection of the pulsar’s semi-major axis a_{PSR} onto the observer’s line of sight $x_{\text{PSR}} = a_{\text{PSR}} \sin i / c$ (where i is the angle between the orbital angular momentum vector and the line of sight and c is the speed of light), the time of periastron T_0 and the longitude of periastron ω .

For each new pulsar, these parameters are determined by fitting a radial velocity model to the observed spin periods, which are Doppler shifted by the orbital motion of the pulsar. This is similar to what can be done in spectroscopic systems. The unique feature of pulsars is that, by determining the correct rotational phase count, one can directly *range* the pulsar relative to the center of mass of the system. Measuring a pulse time of arrival with a precision of $1 \mu\text{s}$ translates into a ranging accuracy of 300 m per measurement, which is much smaller than the astronomical sizes of the orbits. This provides Keplerian parameters many orders of magnitude more precise than those derived from Doppler shift measurements with the same data and is the reason why pulsars are so useful for such a wide variety of purposes - including uniquely precise mass measurements.

The binary mass function is then determined from the Keplerian orbital parameters

$$f = \frac{(M_c \sin i)^3}{M_{\text{T}}^2} = \frac{4\pi^2}{T_{\odot}} \frac{x_{\text{PSR}}^3}{P_b^2}, \quad (1)$$

where $T_{\odot} \equiv GM_{\odot}/c^3 = 4.925490947 \mu\text{s}$ is the mass of the Sun in time units², and M_{PSR} , M_c and $M_{\text{T}} = M_{\text{PSR}} + M_c$ are the pulsar, companion and total binary masses, respectively, all expressed in solar masses. This single equation has three unknowns (i , M_{PSR} and M_c); therefore, in the absence of further information, the individual masses M_{PSR} and M_c cannot be determined despite the very high precision in the determination of the Keplerian parameters.

If the projected semi-major axis of the companion’s orbit x_c can be measured, either via timing, if the companion is a pulsar, or via phase-resolved optical spectroscopy, if the companion is a white dwarf or main-sequence star, one extra equation is obtained:

$$q \equiv \frac{M_{\text{PSR}}}{M_c} = \frac{x_c}{x_{\text{PSR}}}, \quad (2)$$

which is valid, to first Post-Newtonian order, in all conservative theories of gravity. The number of binary systems where we can measure q is small, but even for those systems, measuring f and q is not enough to determine the masses. This can be addressed in a few systems since the spectrum of a white dwarf companion allows, in some cases, a determination of its mass, M_{WD} (see section 2.3.3).

Because of the small sizes of neutron stars and their neutron star or white dwarf companions compared to their orbits, both components can be treated as point masses. In this case, the “classical” tidal and rotational effects that complicate the motion of other astrophysical objects and hide the (generally smaller) relativistic effects are simply absent, i.e., such systems are clean gravitational laboratories. In such a system, a pulsar with good timing precision will allow the detection and

²The product GM_{\odot} , where G is Newton’s gravitational constant and M_{\odot} is the solar mass is very precisely known, despite the fact that neither G nor M_{\odot} are individually known to better than one part in 10^3 .

precise measurement of these small relativistic effects. These effects can be parameterized by “post-Keplerian” (PK) parameters, which, assuming that general relativity (GR) is the correct theory of gravity, and to leading post-Newtonian order, are related to three of the Keplerian parameters (P_b , x and e) and the system masses. For the five PK parameters that have been measured in the context of pulsar timing, these expressions are as follows (as in Stairs 2003 and references therein):

1. The rate of advance of periastron $\dot{\omega}$, typically measurable in eccentric orbits. This is analogous to the anomalous perihelion advance in Mercury’s orbit:

$$\dot{\omega} = 3 \left(\frac{P_b}{2\pi} \right)^{-5/3} (T_\odot M_T)^{2/3} (1 - e^2)^{-1}. \quad (3)$$

2. The “Einstein delay”, γ . In GR, this is due in equal parts to the variations of the gravitational redshift and of special relativistic time dilation in an eccentric orbit:

$$\gamma = e \left(\frac{P_b}{2\pi} \right)^{1/3} T_\odot^{2/3} M_T^{-4/3} M_c (M_{\text{PSR}} + 2M_c). \quad (4)$$

3. The orbital period decay \dot{P}_b due to the loss of orbital energy of the system caused by the emission of gravitational waves (this typically requires timing observations that span many years),

$$\dot{P}_b = -\frac{192\pi}{5} \left(\frac{P_b}{2\pi T_\odot} \right)^{-5/3} \left(1 + \frac{73}{24}e^2 + \frac{37}{96}e^4 \right) \times (1 - e^2)^{-7/2} M_{\text{PSR}} M_c M_T^{-1/3}. \quad (5)$$

4. The range r and the shape s of Shapiro delay, which is a delay in the reception of the radio pulses at the Earth that is due to the propagation of the radio signal in the curved space-time near the companion star

$$r = T_\odot M_c, \quad (6)$$

$$s = \sin i = x_{\text{PSR}} \left(\frac{P_b}{2\pi} \right)^{-2/3} T_\odot^{-1/3} M_T^{2/3} M_c^{-1}. \quad (7)$$

This effect is more easily detected in edge-on orbits.

We must here emphasize that, like the Keplerian parameters, these are parameters that appear in the equations that describe the motion and timing of binary pulsars, such as those presented in Damour & Deruelle (1985, 1986). They are measured by timing a particular system and fitting the pulse arrival times. It is only when we adopt a specific theory of gravity that we can relate them to physical parameters of the components of the binary - in the case of GR, and to leading PN order, their masses only (eqs. 3 - 7). These constraints are displayed graphically in Fig. 1. Note that there is nothing unique about the particular parameterization of Damour & Deruelle (1985). As an example, instead of r and s , we can describe Shapiro delay with two less correlated PK parameters ς and h_3 (Freire & Wex 2010).

2.2. Double neutron star mass measurements

The first system for which reliable mass measurements were made was PSR B1913+16, the first binary pulsar ever discovered (Hulse & Taylor 1975). The compact orbit of this double neutron star system ($P_b = 0.32299$ days) and its high orbital eccentricity ($e = 0.6171334(5)$) allowed a precise measurement of the PK parameter $\dot{\omega}$. Subsequently, Taylor, Fowler & McCulloch (1979) were able to measure two more PK parameters, γ and \dot{P}_b . The individual masses were determined from Eqs. 3

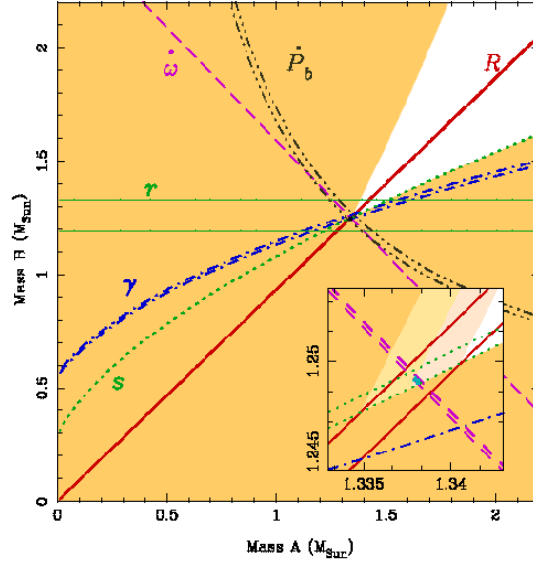


Figure 1

Mass-mass diagram for the J0737–3039 system. The yellow areas are excluded by the mass functions of both pulsars, PSRs J0737–3039A and B. The lines represent the regions allowed by eqs. 2 to 7 for the measured PK parameters. All lines meet at a single point in the diagram, i.e., GR passes the tests posed by these four distinct constraints. For our purposes, this plot is very important since it indicates that we get consistent mass measurements using any pair of PK parameters. From Kramer et al. 2006.

and 4 and the observed orbital decay was then used as a successful test of GR. The GR prediction for \dot{P}_b caused by gravitational wave emission (Eq. 5) for the derived masses was consistent observed rate (see Damour 2015 for a review).

A number of other double neutron systems (DNSs) have since been discovered. The eleven systems for which mass constraints are known are listed in the top two groups in Table 1, together with the latest references. These systems are relatively rare, about 5% of the currently known population of binary pulsars. We list the total mass M_T of each binary since, generally, that is much better known than the individual masses of the components. This happens because the orbits of all double neutron stars are eccentric, so that $\dot{\omega}$ (and M_T) can be determined with high precision. In binaries where additional PK parameters are measured, we also list the individual NS masses and specify the parameters that were measured to derive the masses (for all these systems, Eq. 1 can be used to determine the orbital inclination i). For one of these systems – J1906+0746 – it is possible for the companion to be a massive WD instead. PSR B2127+11C is located in the globular cluster M15 and is very likely the result of an exchange interaction (Prince et al. 1991; Lynch et al. 2012).

PSR B1913+16 is no longer unique in providing a stringent test of general relativity. The orbital decay due to the emission of gravitational waves has been measured for *five* other DNS systems (J0737–3039A/B, B1534+12, J1756–2251, J1906+0746 and B2127+11C), and, as we will discuss below, a few millisecond pulsar-white dwarf systems as well.

We also include in Table 1 two radio pulsars that have precise mass measurements even though they are not members of DNS systems. Their slow spins and higher magnetic fields indicate that they have not been recycled, making them resemble DNSs rather than the millisecond pulsars with

Table 1 Masses of Double Neutron Star Systems and Non-recycled Pulsars

System	M_T (M_\odot)	M_{PSR} (M_\odot)	M_c (M_\odot)	Mass const.	Ref.
Systems with well-measured component masses					
J0453+1559	2.734(4)	1.559(5)	1.174(4)	$\dot{\omega}, h_3$	1,2
J0737–3039	2.58708(16)	1.3381(7)	1.2489(7) y	$\dot{\omega}, q$	3
B1534+12	2.678463(8)	1.3330(4)	1.3455(4)	$\dot{\omega}, \gamma$	4
J1756–2251	2.56999(6)	1.341(7)	1.230(7)	$\dot{\omega}, \gamma$	5
J1906+0746	2.6134(3)	1.291(11) y	1.322(11) ?	$\dot{\omega}, \gamma$	6
B1913+16	2.828378(7)	1.4398(2)	1.3886(2)	$\dot{\omega}, \gamma$	7
B2127+11C g	2.71279(13)	1.358(10)	1.354(10)	$\dot{\omega}, \gamma$	8
Systems with total binary mass measurement only					
J1518+4904	2.7183(7)	<1.768	>0.950	$\dot{\omega}$	9
J1811–1736	2.57(10)	<1.64	>0.93	$\dot{\omega}$	10
J1829+2456	2.59(2)	<1.34	>1.26	$\dot{\omega}$	11
J1930–1852	2.59(4)	<1.32	>1.30	$\dot{\omega}$	12
Non-recycled pulsars with massive WD companions					
J1141–6545	2.2892(3)	1.27(1) y	1.01(1)	$\dot{\omega}, \gamma$	14,15
B2303+46	2.64(5)	1.24–1.44 y	1.4–1.2	$\dot{\omega}, M_{\text{WD}}$	15,16

Notes: The systems indicated with a “g” are located in globular clusters. A question mark indicates that the NS nature of the companion is not firmly established. The mass measurements for neutron stars detected as normal (non-recycled) radio pulsars are indicated with the letter “y”. References are to the latest mass measurements: 1. Deneva et al. (2013) 2. Martinez et al. (2015) 3. Kramer et al. (2006) 4. Fonseca, Stairs & Thorsett (2014) 5. Ferdman et al. (2014) 6. van Leeuwen et al. (2015) 7. Weisberg, Nice & Taylor (2010) 8. Jacoby et al. (2006) 9. Janssen et al. (2008) 10. Corongiu et al. (2007) 11. Champion et al. (2005) 12. Swiggum et al. (2015) 13. Bhat, Bailes & Verbiest (2008) 14. Antoniadis et al. (2011) 15. Thorsett & Chakrabarty (1999) 16. van Kerkwijk & Kulkarni (1999)

white dwarf companions that we discuss in Section 2.3.

2.2.1. The double pulsar. Among the DNS population, one system in particular stands out: J0737–3039. This system is a unique laboratory for gravitational physics because it combines an unusual number of desirable features: (i) With an orbital period of 2h 27m, it is by far the most compact DNS known. Combined with the moderate orbital eccentricity of the system, this implies that the PK parameters $\dot{\omega}$, γ and \dot{P}_b are relatively large and will be easy to measure, promising one precise test of GR. (ii) The system has a very high orbital inclination, $\sim 89^\circ$. This allows for a very precise measurement of the two Shapiro delay parameters, r and s , thus providing two more independent tests of GR. (iii) The second neutron star in the system is also an active radio pulsar, which is detectable at least some of the time (Lyne et al. 2004). This makes it the only currently known *double pulsar* system and allows a precise measurement of the mass ratio, q , which “frees” one of the PK parameters from the role of mass determination and, therefore, allows one more test of GR.

The four tests in this system provided by eqs. 3 - 7 are remarkably stringent, but despite that, GR has passed all of them (Kramer et al. 2006). This can be seen in Fig. 1, where all the regions compatible with the known mass constraints are consistent with the same pair of masses. Such tests of gravity theories are not the topic of this review — we refer interested readers to Wex (2014) for a comprehensive discussion. Nevertheless, systems like J0737–3039 and Fig 1 are important for NS mass measurements because they demonstrate experimentally that any pair of mass constraints chosen from q and the PK parameters will generally yield consistent NS masses.

Table 2 Masses of Millisecond Pulsars

System	M_{T} (M_{\odot})	M_{PSR} (M_{\odot})	M_{c} (M_{\odot})	Mass const.	Ref.
MSPs with WD companions and low-eccentricity orbits					
J0348+0432	2.32(8)	2.01(4)	0.172(3)	q, M_{WD}	Antoniadis et al. (2013)
J0437−4715		1.44(7)	0.224(7)	r, s	Reardon et al. (2016)
J0621+1002		$1.53^{+0.10}_{-0.20}$	$0.76^{+0.28}_{-0.07}$	$\dot{\omega}, s$	Kasian (2012)
J0751+1807		1.72(7)	0.13(2)	s, \dot{P}_b	Desvignes et al. (2016)
J1012+5307		1.83(11)	0.16(2)	q, M_{WD}	Antoniadis et al. (2016)
J1614−2230	2.57190(73)	1.928(17)	0.500(6)	r, s	Fonseca et al. (2016)
J1713+0747		1.31(11)	0.286(12)	r, s	Zhu et al. (2015)
J1738+0333		$1.47^{+0.07}_{-0.06}$	$0.181^{+0.007}_{-0.005}$	q, M_{WD}	Antoniadis et al. (2012)
J1802−2124		1.24(11)	0.78(4)	r, s	Ferdman et al. (2010)
J1807−2500B		1.3655(21)	1.2064(20)(?)	$\dot{\omega}, h_3$	Lynch et al. (2012)
B1855+09	2.57190(73)	1.58^{+10}_{-13}	$0.267^{+0.010}_{-0.014}$	r, s	Splaver (2004)
J1909−3744		1.47(3)	0.2067(19)	r, s	Reardon et al. (2016)
J2222−0137		1.20(14)	1.05(6)	r, s	Kaplan et al. (2014a)
MSPs with eccentric orbits and triples					
J0337+1715	2.697(29)	1.4378(13)	0.19751(15)	i, q	Ransom et al. (2014); Kaplan et al. (2014b)
J1903+0327			0.4101(3)	$\dot{\omega}, h_3$	Freire et al. (2011)
J1946+3417			1.029(8)	$\dot{\omega}, h_3$	Barr et al. (2016)
J2234+0611			0.2659(30)	$\dot{\omega}, h_3$	Stovall & et al. (2015)
MSPs in globular clusters					
J0024−7204H	1.61(4)	< 1.52	> 0.164	$\dot{\omega}$	Freire et al. (2003)
J0514−4002A	2.453(14)	< 1.50	> 0.96	$\dot{\omega}$	Freire, Ransom & Gupta (2007)
B1516+02B	2.29(17)	< 2.52	> 0.13	$\dot{\omega}$	Freire et al. (2008a)
J1748−2021B	2.92(20)	< 3.24	> 0.11	$\dot{\omega}$	Freire et al. (2008b)
J1748−2446I	2.17(2)	< 1.96	> 0.24	$\dot{\omega}$	Ransom et al. (2005)
J1748−2446J	2.20(4)	< 1.96	> 0.38	$\dot{\omega}$	Ransom et al. (2005)
J1750−37A	1.97(15)	< 1.65	> 0.53	$\dot{\omega}$	Freire et al. (2008b)
B1802−07	1.62(7)	< 1.7	> 0.23	$\dot{\omega}$	Thorsett & Chakrabarty (1999)
J1824−2452C	1.616(7)	< 1.35	> 0.26	$\dot{\omega}$	Bégin (2006)
J1910-5958A		1.3(2)	0.180(18)	q, M_{WD}	Bassa et al. (2006); Cocozza et al. (2006)

Notes: J1807−2500B is located in the globular cluster NGC6544. A question mark indicates that the nature of the companion is uncertain. The total mass is indicated only when it is known more precisely than the masses of the components. References are to the latest mass measurements.

2.3. Millisecond pulsars

The term “millisecond pulsars” (MSPs) refers to pulsars with spin periods in the range $1.39 < P < 20$ ms and $\dot{P} < 10^{-19}$. These systems have been heavily recycled (and circularized) by a long-lived accretion phase in a low-mass X-ray binary (LMXB). The first MSP by this definition, B1937+21, was discovered at the Arecibo telescope in 1982 (Backer et al. 1982). (At a 642 Hz spin frequency, this was the fastest known MSP for the subsequent 24 years.) A very large number of MSPs have been discovered since and, although $\sim 20\%$ are isolated, most of the remaining objects have white dwarf companions and very small orbital eccentricities.

The fast (and very stable) rotation of MSPs makes their timing significantly more precise than for the pulsars in DNSs. However, their low orbital eccentricities pose a problem for mass

determination (and tests of GR), since, in these cases, the PK parameters $\dot{\omega}$ and especially γ cannot be measured accurately. Furthermore, most systems have orbital periods larger than 0.5 d, which makes a detection of the very small predicted \dot{P}_b nearly impossible. These difficulties made the measurement of MSP masses a slow and difficult process. Four strategies have been followed over the last two decades, which have recently started producing a number of precise mass measurements.

2.3.1. Pulsars in globular clusters. One way of getting around the issue of orbital circularity is to find MSPs in globular clusters (GCs). Because of the much higher stellar density, there are substantial gravitational interactions with nearby stars that, with time, can make an initially circular orbit acquire a substantial eccentricity. This allows the measurement of $\dot{\omega}$ and, if there are no classical contributions to this effect, the total mass of the system M_T for quite a few systems (see Table 2).

The first binary mass precise enough to be useful was that of PSR J0024–7204H, a 3.21 ms pulsar in a 2.35-day, slightly eccentric ($e = 0.070560(3)$) orbit around a low-mass WD in the globular cluster 47 Tucanae, which yielded $M_T = 1.61 \pm 0.04 M_\odot$ (Freire et al. 2003). No further PK parameters were measurable; nevertheless, one can infer from combining Eqs. 1 and 3 (and the mathematical fact $\sin i \leq 1$) that $M_{\text{PSR}} < 1.52 M_\odot$. This was one of the earlier indications that the long recycling episodes that spin up MSPs do not necessarily make them very massive.

Most eccentric systems discovered since in GCs share the same characteristic: we can measure $\dot{\omega}$ but no other mass constraints. The reason is that the most eccentric systems tend to be the ones with wider orbits, which are easier to perturb by nearby stars. For these relatively wide orbits, it is very difficult to measure γ and \dot{P}_b .

The two exceptions are two of the exchange encounter systems B2127+11C and J1807–2500B listed in Tables 1 and 2. Both are located in clusters with collapsed cores, where exchange encounters are more likely (Verbunt & Freire 2014). The orbital period of B2127+11C is 8.0 hr and its orbital eccentricity is 0.681386(16), which allows measurements of $\dot{\omega}$, γ and even \dot{P}_b (Jacoby et al. 2006). The last system, J1807–2500B, is particularly important for this discussion: it is a true MSP with a spin period is 4.18 ms, but despite the long accretion episode, its current mass is only $1.3655(21) M_\odot$. More than any other system, this MSP demonstrates that full recycling can be achieved without a large mass increment.

Nevertheless, as the number of M_T measurements accumulated, it became apparent that some systems, such as PSRs J1748–2446I and J in Terzan 5 (Ransom et al. 2005), PSR J1748–2021B in NGC 6440 (Freire et al. 2008b) and PSR B1516+02B in M5 (Freire et al. 2008a) are quite massive but have very low mass functions. This is only likely to happen if the pulsars and not the companions in these systems are massive. Indeed, by 2008, there was already strong evidence that a fair fraction of MSPs must have masses close to $2 M_\odot$ (Freire et al. 2008a). This statistical results was confirmed by the later MSP mass measurements, described below.

2.3.2. Shapiro delay measurements. For the vast majority of pulsar-WD systems, the only measurable PK parameters are those related to the Shapiro delay. However, the fastest-spinning MSPs tend to have very low-mass helium white dwarf companions, which reduces the amplitude of the Shapiro delay. Therefore, in order to measure the masses in these systems, both a very good timing precision and a high orbital inclination are required.

The first MSP-WD system where the Shapiro delay was clearly detected was PSR B1855+09 (Ryba & Taylor 1991). However, until recently, the timing precision in this system was not enough for a precise determination of the pulsar mass. This changed in 2003 with the discovery of PSR J1909–3744, a heavily recycled MSP with $P = 2.9$ ms and a light helium white dwarf companion (Jacoby et al. 2003). This system combines very high timing accuracy with a very high orbital inclination, which allowed, in 2005, the first precise measurement of the mass of a MSP:

$1.438 \pm 0.024 M_{\odot}$ (Jacoby et al. 2005).

Since then, the number of MSPs discovered has been increasing significantly (see section 5.1), and for that reason the number of precise Shapiro delay mass measurements has been accumulating, particularly for pulsars with more massive carbon-oxygen (CO) or oxygen-neon-magnesium (O-Ne-Mg) white dwarf companions, such as PSR J1802–2124 (Ferdman et al. 2010), or more recently PSR J2222–0137 (Kaplan et al. 2014a). The larger companion masses make the Shapiro delay easier to measure; this is why a disproportionate number of MSPs with well-measured masses have such massive companions. This does not apply as a rule to the MSPs themselves: the latter systems highlight the fact that many NSs are born with masses as low as $\sim 1.2 M_{\odot}$.

Of these MSPs with massive WD companions, the measurement that had by far the greatest impact was PSR J1614–2230 (Demorest et al. 2010). The originally reported mass of the pulsar was $1.97(4) M_{\odot}$, exceptional and unexpected among the MSPs with massive WD companions. This mass measurement had implications for the NS mass distribution as well as for the NS equation of state (EOSs), which will be discussed in later sections. Note that this measurement has since been slightly improved, which revised the mass to $M = 1.928(7) M_{\odot}$ (Arzoumanian et al. 2015), still consistent with the earlier value.

2.3.3. Spectroscopic mass measurements. For some of the MSPs, particularly those with short orbital periods, the companion is optically bright. This has allowed reliable mass determinations of both components by studying the Balmer lines produced by hydrogen in the white dwarf atmosphere.

First, phase-resolved spectroscopy can measure how these lines shift with orbital phase, providing a measurement of the projected orbital velocity of the white dwarf. Comparing this to the orbital velocity of the pulsar measured in the timing ($v_{\text{PSR}} = 2\pi x_{\text{PSR}}/P_b$) we can immediately determine the mass ratio, $q \equiv M_{\text{PSR}}/M_{\text{WD}} = v_{\text{WD}}/v_{\text{PSR}}$.

Second, the width of the Balmer lines is related to the local gravitational acceleration, $g = GM_{\text{WD}}/R_{\text{WD}}^2$. Using model relations between M_{WD} and R_{WD} for white dwarfs (see, e.g., the references in Antoniadis et al. 2012), both quantities can be determined from g . After this step M_{PSR} can be obtained trivially from qM_{WD} .

The first such measurement was made for PSR J1012+5307 (Callanan, Garnavich & Koester 1998), later followed by the mass measurement for J1910–5958A, a MSP-WD system in NGC 6752 (Bassa et al. 2006; Ccozza et al. 2006). To date, the two most important such measurements have been those of J1738+0333 (Antoniadis et al. 2012) and J0348+0432 (Lynch et al. 2013; Antoniadis et al. 2013). For the former $M_{\text{PSR}} = 1.47_{-0.06}^{+0.07} M_{\odot}$ and $M_{\text{WD}} = 0.181_{-0.005}^{+0.007} M_{\odot}$; this measurement was important because the relatively short orbital period (8.5 hr) allowed a measurement of \dot{P}_b (Freire et al. 2012), which agrees with the GR prediction for these masses. Given the asymmetry in the binding energy of this system, this measurement introduced the most stringent constraints ever for several families of gravity theories (Freire et al. 2012), superseding the previous test from the pulsar - WD system PSR J1141–6545 (Bhat, Bailes & Verbiest 2008).

For PSR J0348+0432, a pulsar with a WD companion with an orbital period of only 2hr 27m, Antoniadis et al. (2013) obtained $M_{\text{PSR}} = 2.01(4) M_{\odot}$ and $M_{\text{WD}} = 0.172(3) M_{\odot}$. This confirmed, using a different method, that neutron stars could reach masses of the order of $2 M_{\odot}$. Furthermore, the very short orbital period has allowed a measurement of \dot{P}_b (Antoniadis et al. 2013), which again agrees with the GR prediction and has already placed significant constraints on non-linear phenomena predicted by some alternative theories of gravity for these massive NSs, such as spontaneous scalarization (Damour & Esposito-Farèse 1996).

2.3.4. Triples, disrupted triples, and other monsters. The theoretical expectation that the recycling pathway for fast MSPs result in highly circular orbits was corroborated by the fact that all fully recycled MSPs outside of globular clusters observed until 2008 had orbital eccentricities between 10^{-7} and 10^{-3} (Manchester et al. 2005). In 2008, the situation changed with the discovery of PSR J1903+0327 (Champion et al. 2008). This fast-spinning MSP ($P = 2.15$ ms) is in binary system with a $\sim 1 M_{\odot}$ main-sequence star companion in a 95-day, eccentric orbit ($e = 0.44$). This system is thought to have originated from a hierarchical triple that became chaotically unstable, as suggested by observational data (Freire et al. 2011) and numerical simulations (Portegies Zwart et al. 2011). This finding suggested triple stellar systems containing MSPs might still be found in the Galaxy, which was later confirmed with the discovery of PSR J0337+1715, the first MSP in a stellar triple system with two white dwarf companions (Ransom et al. 2014). Note that the mass indicated in Table 2 for PSR J0337+1715 is based on these triple interactions.

Soon after the discovery of PSR J1903+0327, Bailes (2010) reported an “anomalous” orbital eccentricity of 0.027 for PSR J1618–3919, a 12-ms pulsar first reported in Edwards & Bailes (2001) that is in a 22-day orbit with a low-mass white dwarf companion. More recently, Deneva et al. (2013), Barr et al. (2013), Knispel et al. (2015), and Camilo et al. (2015) reported the discovery of four more unusual binary MSP systems with eccentric orbits: PSRs J2234+06, J1946+3417, J1950+2414, and J0955–6150. These four systems are fully recycled with spin periods between 2 and 4.4 ms, orbital periods from 22 to 32 d and median companion masses $M_c \approx 0.25 M_{\odot}$; i.e., apart from their large orbital eccentricities ($0.07 < e < 0.14$) all parameters are compatible with the canonical recycling formation channel leading to a MSP with a white dwarf companion. For a discussion on their unusual formation, see Knispel et al. (2015).

The reason why these systems are mentioned at length here is that for nearly all of them, precise mass measurements have been, or will soon be, made. For PSR J1903+0327, PSR J1946+3417, and J2234+0611 precise mass measurements have been obtained from the combination of $\dot{\omega}$ and the Shapiro delay parameter h_3 (Freire et al. 2011; Barr et al. 2016; Stovall & et al. 2015). Note that for PSR J1903+0327, the uncertainty quoted in Table 2 corresponds to 99.7% confidence level. The same will certainly be possible for PSR J1950+2414. For the triple system, even more precise masses for the MSP and two white dwarf companions could be obtained from the 3-body effects in the system (Ransom et al. 2014).

The masses in these systems are quite varied. While the MSP in the triple system J0337+1715 and J2234+0611 have masses of $1.4378(13) M_{\odot}$ and $1.393(13) M_{\odot}$, respectively, PSR J1946+3417 is in the massive neutron star group, with $M_{\text{PSR}} = 1.912(10) M_{\odot}$ (Barr et al. 2015, in preparation). PSR J1903+0327 sits in the middle, with $M_{\text{PSR}} = 1.667(21) M_{\odot}$ (99.7% C. L.)³

2.4. Neutron Stars in X-ray Binaries

Mass measurements have also been carried out for neutron stars with high and low stellar mass companions using the observations of these binaries in X-ray and optical wavelengths. We discuss the methods and results for these two classes below.

2.4.1. Neutron Stars with High-Mass Companions. For mass measurements of neutron stars with high-mass companions, eclipsing X-ray pulsars, in which the companions block the X-rays from the pulsar for part of the orbit, form the primary targets. In these systems, X-ray observations of the pulsar yield the orbital period of the binary P_b , the eccentricity of the orbit e , longitude of

³The error bars for this measurement are not Gaussian, therefore the 68% error bar is not 1/3 of this uncertainty. See the original reference for a discussion.

Table 3 Masses of Neutron Stars in High-Mass and Low-Mass X-ray Binaries

System	M_{NS} (M_{\odot})	Error (M_{\odot})	References
Neutron Stars in High-Mass X-ray Binaries			
LMC X-4	1.57	0.11	1
Cen X-3	1.57	0.16	1
4U 1538-522	1.02	0.17	1
SMC X-1	1.21	0.12	1
SAX J1802.7-2017	1.57	0.25	1
XTE J1855-026	1.41	0.24	1
Vela X-1	2.12	0.16	1
EXO 1722-363	1.91	0.45	1
OA0 1657-415	1.74	0.30	1
Her X-1	1.07	0.36	1
Neutron Stars in Low-Mass X-ray Binaries			
4U 1608-52	1.57	$+0.30$ -0.29	2
4U 1724-207	1.81	$+0.25$ -0.37	2
KS 1731-260	1.61	$+0.35$ -0.37	2
EXO 1745-248	1.65	$+0.21$ -0.31	2
SAX J1748.9-2021	1.81	$+0.25$ -0.37	2
4U 1820-30	1.77	$+0.25$ -0.28	2
Cyg X-2	1.90	$+0.22$ -0.35	3

Notes. 1. See Falanga et al. (2015), Özel et al. (2012), Rawls et al. (2011), and references therein. We exclude 4U 1700-377, for which there is no evidence that it is a neutron star. 2. See Özel et al. (2015) for the latest constraints. 3. Orosz & Kuulkers (1999).

periastron ω_0 , the semi-major axis of the neutron star's orbit $a_X \sin i$, and the semi-duration of the eclipse θ_e . In addition, optical observations of the companion star give its velocity amplitude K_{opt} , its projected rotational velocity $v_{\text{rot}} \sin i$, and the amplitude of ellipsoidal variations A . From these observables, it is possible to solve for the fundamental parameters of the binary, which include the mass of the neutron star M_{NS} , the mass, radius and rotational angular velocity of the companion, M_{opt} , R_{opt} , Ω_{opt} , and the inclination angle of the binary i .

These measurements are typically less precise than those obtained from radio pulsar timing, and several sources of systematic uncertainty in this technique have been discussed in Özel et al. (2012) and Falanga et al. (2015). The ten neutron stars whose masses have been estimated in this way are listed in Table 3.

2.4.2. Neutron Stars in Low-Mass X-ray Binaries. Spectral studies of thermonuclear X-ray bursts from neutron stars provide simultaneous measurements of their masses and radii. These mass constraints are less precise than those obtained from pulsar timing but still provide an estimate of neutron star masses in a different population. The details of the methods will be discussed in Section 3.1 and the mass measurements for the six sources in this category are listed in Table 3. This table also includes the low-mass X-ray binary Cyg X-2, for which the mass of the neutron star was inferred using optical observations of its companion.

2.5. Neutron Star Mass Distribution

We show in Figure 2 the combined neutron star mass measurements in all of the above categories. It is already clear from this figure that current measurements show a broad range of neutron star

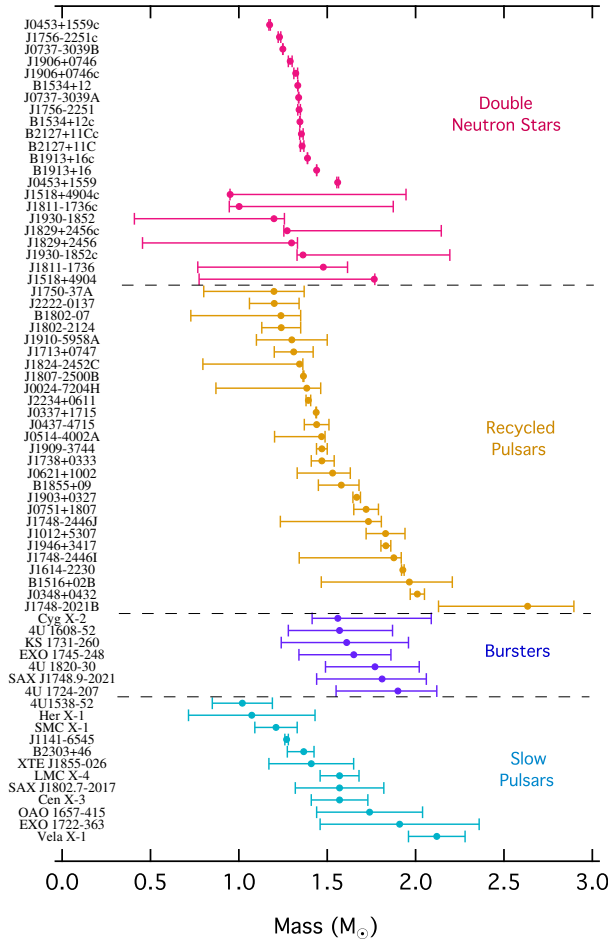


Figure 2

The most recent measurement of neutron star masses. Double neutron stars (magenta), recycled pulsars (gold), bursters (purple), and slow pulsars (cyan) are included.

masses, from $\approx 1.1 - 2 M_\odot$. The differences between the neutron star masses in different categories are also evident. To study and characterize the mass distributions of these different classes in more detail, it is possible to use Bayesian statistical techniques on the currently available measurements. In particular, the three different categories of sources, namely, the DNSs, the slow pulsars (i.e., the small spin period pulsars and neutron stars with high mass companions, which are likely to be near their birth masses) and the recycled pulsars (which include all MSPs and the accreting neutron stars with low-mass companions) can each be modeled with Gaussian functions with a mean of M_0 and a dispersion σ

$$P(M_{\text{NS}}; M_0, \sigma) = \frac{1}{\sqrt{2\pi\sigma^2}} \exp \left[-\frac{(M_{\text{NS}} - M_0)^2}{2\sigma^2} \right]. \quad (8)$$

Several studies have employed Bayesian techniques to measure the most likely values of the mean and dispersion for these systems (Özel et al. 2012; Kiziltan et al. 2013). Fig. 3 shows the inferred mass distributions for these different categories of neutron stars. The most likely values of the

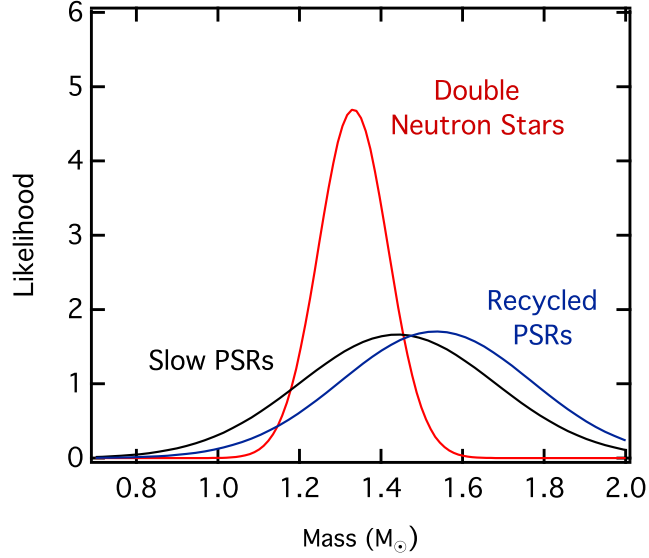


Figure 3

The inferred mass distributions for the different populations of neutron stars.

parameters for these distributions are: $M_0 = 1.33 M_\odot$ and $\sigma = 0.09 M_\odot$ for the DNSs, $M_0 = 1.54 M_\odot$ and $\sigma = 0.23 M_\odot$ for the recycled neutron stars, and $M_0 = 1.49 M_\odot$ and $\sigma = 0.19 M_\odot$ for the slow pulsars. A recent study also raised the possibility of two peaks within the recycled millisecond pulsar population, with the first peak at $M = 1.388 M_\odot$ and a dispersion $\sigma = 0.058 M_\odot$ and a second peak appearing at $M = 1.814 M_\odot$ with a dispersion of $\sigma = 0.152 M_\odot$ (Antoniadis et al. 2016).

Among these inferred distributions, the narrowness of the DNS distribution stands out. While clearly not representative of neutron stars as a whole, as it was once thought (Thorsett & Chakrabarty 1999), it probably points to a particular evolutionary mechanism that keeps the masses of neutron stars in these systems in a narrow range. Recent discoveries, such as the DNS J0453+1559 (Deneva et al. 2013), indicate that the range of masses in double neutron-star systems may also be wider than previously believed: the recycled pulsar has a mass of $1.559(5) M_\odot$, the heaviest known in any DNS (Martinez et al. 2015), while the companion has a mass of $1.174(4) M_\odot$, the smallest precisely measured mass for any NS (We infer that the companion is a NS from the orbital eccentricity of the system, $e = 0.11251837(5)$, which would not arise if it had slowly evolved to a massive white dwarf star).

2.6. Maximum Mass of Neutron Stars

Finding the maximum mass of neutron stars is of particular interest in mass measurements because of its direct implications for the neutron star equation of state and neutron star evolution. The largest neutron star mass can rule out the equations of state that have maximum masses that fall below this value. The current record holder on this front is J0348+0432 with a mass of $2.01 \pm 0.04 M_\odot$ (Antoniadis et al. 2013).

There are also some studies of a particular class of millisecond pulsars called black widows (and their cousins redbacks) that have suggested higher neutron star masses (e.g.,

van Kerkwijk, Breton & Kulkarni 2011). These millisecond pulsars irradiate and ablate their very low-mass companions. While the pulsar timing provides the Keplerian parameters for the orbit, all other information about the masses in these systems is obtained from the modeling of the optical lightcurves (to determine orbital inclination) and the spectroscopy (to measure the mass ratio) of the companion star. Unfortunately, there are many difficulties in obtaining accurate measurements from these ablated companions. Even when using a model of an irradiated companion, the short timescale variability, the unevenly heated surface, and the observed asymmetry in the lightcurves significantly hinder the orbital inclination measurements. Similarly, the difference between the center of light of the irradiated companion and its center of mass as well as the departure of the spectral features from assumptions of thermodynamic equilibrium introduce large uncertainties in the inferred mass ratios (Roberts et al. 2015). These results are tantalizing and hint at the possibility of even more massive neutron stars than J0348+0432, but because of the systematics, we find that they are not yet as robust as the results from radio timing.

3. RADIUS MEASUREMENTS

Neutron star radius measurements have progressed significantly in the past decade and a number of different techniques have been employed. Nearly all of the methods that are currently used rely on the detection of thermal emission from the surface of the star either to measure its apparent angular size or to detect the effects of the neutron-star spacetime on this emission to extract the radius information. The approaches can broadly be divided into spectroscopic and timing measurements. In addition, there are proposed methods for determining neutron star radii which show promise for the future but will not be covered in this review, because there are currently limited data, or because they provide only broad limits:

1. Quasi-periodic oscillations observed from accreting neutron stars (e.g., Miller, Lamb & Psaltis 1998)
2. Neutron star cooling (e.g., Page & Reddy 2006)
3. Pulsar glitches, which help constrain the relative thicknesses of neutron star crust vs. its core (e.g., Link, Epstein & Lattimer 1999)
4. Asteroseismology (e.g., Watts et al. 2015)

3.1. Spectroscopic measurements

Much like measuring the radii of normal stars, spectroscopic measurements of neutron star radii rely on determining their angular sizes by measuring a thermal flux F , modeling the spectrum to determine the effective temperature T_{eff} , and combining this with a distance measurement D to obtain observed (or apparent) radii

$$\frac{R_{\text{obs}}}{D} = \left(\frac{F_{\text{bol}}}{\sigma_{\text{B}} T_{\text{eff}}} \right)^{1/2}, \quad (9)$$

where σ_{B} is the Stefan-Boltzmann constant. Unlike stars, however, there are several complications that come into play in this process. First, owing to their extreme compactness, neutron stars gravitationally lense their own surface emission. This introduces mass-dependent corrections to the observed angular sizes (Pechenick, Ftaclas & Cohen 1983; Psaltis, Özel & DeDeo 2000), i.e., the physical radii are related to the observed radii via

$$R_{\text{obs}} = \left(1 - \frac{2GM}{Rc^2} \right)^{-1/2} R. \quad (10)$$

(This equation holds as long as the radius is larger than the photon orbit $3GM/c^2$. If it is smaller, then the geometric radius observed at infinity would be equal to $\sqrt{27}GM/c^2$, independent of the stellar radius.) The situation is even more complex in the case of neutron stars that spin moderately fast, because their spacetime can no longer be described by a Schwarzschild metric and there are further spin-dependent corrections to the observed angular sizes (Bauböck et al. 2015). Second, the surface emission may be contaminated by non-thermal emission from an isolated neutron star’s magnetosphere or by the disk surrounding an accreting one. Third, the magnetic field a neutron star possesses can be strong enough to cause temperature non-uniformity on the surface, which complicates the inference of the true stellar radius. Fourth, distances to neutron stars are, in general, more difficult to measure than to normal stars.

Some of these challenges are overcome by detailed theoretical modeling of emission from neutron stars in general relativity. Others are mitigated or eliminated by careful source selection (e.g., sources with low magnetic fields, with low accretion luminosities, or located in globular clusters with known distances) and by combining multiple observational phenomena to break the inherent degeneracies between neutron star mass and radius and to reduce the measurement uncertainties. With these criteria as a guide, thermal emission from low-mass X-ray binaries in quiescence and during X-ray bursts have been the focus of recent work on neutron star radii.

3.1.1. Quiescent Low-mass X-ray Binaries. The first group of sources on which radius measurement efforts have focused on are the accreting neutron stars in low-mass X-ray binaries when they are in quiescence (qLMXBs).

In quiescence, accretion ceases or continues at a very low level. This allows observations of the thermal emission from the stellar surface, which is powered by the reradiation of the heat stored in the deep crust during the accretion phases (Brown, Bildsten & Rutledge 1998). Because of the very short (\sim mins) settling time of heavier elements in the surface layers of neutron stars (Brown, Bildsten & Chang 2002), the atmospheres of neutron stars in quiescence are expected to be composed of hydrogen. (There are cases where the companion is hydrogen poor and a helium atmosphere may be appropriate; see below). The observed spectra of qLMXBs are indeed quasi-thermal, with a weak power-law component at high energies that is likely due to residual accretion.

A number of qLMXBs in globular clusters has been observed with *Chandra* and *XMM-Newton*. Their luminosities in quiescence are of the order of 10^{32-33} erg s $^{-1}$, making them very faint objects. In addition, the globular cluster environments entail crowded fields. Because of this, the high angular resolution and low background of the modern X-ray instruments were crucial for obtaining spectroscopic constraints of their apparent angular sizes (e.g., Rutledge et al. 2001; Heinke et al. 2006; Webb & Barret 2007).

To make quantitative measurements from the observed spectra, radiative equilibrium models of neutron star atmospheres (Zavlin, Pavlov & Shibano 1996; Heinke et al. 2006) have been developed for a variety of surface compositions, surface gravities and temperatures (for a recent review, see Özel 2013). Owing to the low magnetic field strengths of neutron stars in low-mass X-ray binaries (Psaltis & Chakrabarty 1999 and references therein), and the expectation of hydrogen atmospheres, unmagnetized hydrogen models have primarily been used in the spectral analyses to obtain observed angular sizes.

To date, reliable radius constraints have been obtained for eight qLMXBs located in the globular clusters M13, M28, M30, ω Cen, NGC 6304, NGC 6397, and two in 47 Tuc (Heinke et al. 2006; Webb & Barret 2007; Guillot, Rutledge & Brown 2011; Bogdanov et al. 2016). The observed (apparent) angular sizes obtained for these sources have been combined with globular cluster distances (Harris 1996; Guillot & Rutledge 2014; Heinke et al. 2014) to measure their apparent radii. Under somewhat different assumptions, there have been several combined analyses of these measurements

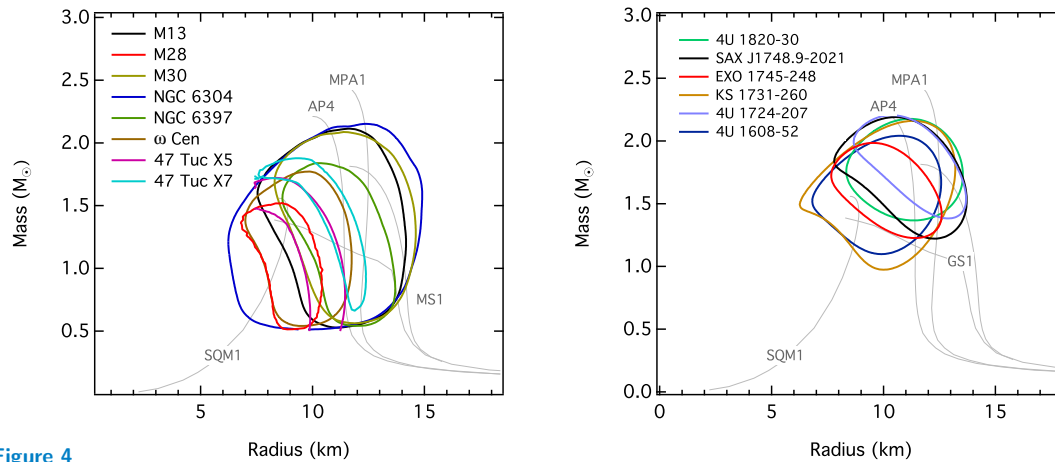


Figure 4 The combined constraints at the 68% confidence level over the neutron star mass and radius obtained from (Left) all neutron stars in low-mass X-ray binaries during quiescence (Right) all neutron stars with thermonuclear bursts. The light grey lines show mass-relations corresponding to a few representative equations of state (see Section 4.1 and Fig. 7 for detailed descriptions.)

(Guillot et al. 2013; Guillot & Rutledge 2014; Lattimer & Steiner 2014; Özel et al. 2015). The most recent results are displayed as correlated contours on the neutron-star mass-radius diagram⁴ (see Fig. 4).

Several sources of systematic uncertainties that can affect the radius measurements have been studied, which we discuss in some detail below.

Atmospheric Composition. The majority of qLMXBs for which optical spectra have been obtained show evidence for H α emission (Heinke et al. 2014), indicating a hydrogen rich companion. Although none of these spectra have been obtained for globular cluster qLMXBs, assuming that sources in globular clusters have similar companions to those in the field led to the use of hydrogen atmospheres when modeling quiescent spectra. There is one source among the six that have been analyzed in detail, for which there is evidence to the contrary. There is only an upper limit on the H α emission from the qLMXB in NGC 6397 using HST observations (Heinke et al. 2014). Because of this, this source has been modeled with a helium atmosphere and the corresponding results are displayed in Fig. 4.

Non-thermal Component. Assuming different spectral indices in modeling the none-thermal spectral component also has a small effect on the inferred radii (Heinke et al. 2014). The low counts in the spectra do not allow an accurate measurement of this parameter; however, a range of values have been explored in fitting the data.

Interstellar Extinction. Because of the low temperature of the surface emission from qLMXBs, the uncertainty in the interstellar extinction has a non-negligible effect on the spectral analyses. Different amounts of interstellar extinction have been assumed in different studies (Guillot et al. 2013; Lattimer & Steiner 2014). A recent study explored different models for the interstellar extinction

⁴The full mass-radius likelihoods and tabular data for these sources can be found at <http://xtreme.as.arizona.edu/NeutronStars>.

in the analysis of the qLMXBs in ω Cen and NGC 6397 and found statistically consistent results with small differences in the central values but larger differences in the uncertainties (Heinke et al. 2014). The relevant uncertainties have been incorporated into the results shown in Fig. 4.

3.1.2. Thermonuclear Bursts. Neutron stars in low-mass X-ray binaries show a phenomenon called thermonuclear (Type-I) X-ray bursts, in which the accreted material undergoes a helium flash that consumes the fuel that is spread over the neutron star surface. The observed X-ray luminosity rises rapidly, in a timescale of ≈ 1 s, which corresponds to the diffusion timescale from the burning layer to the neutron star surface. The energy is then radiated away on a timescale of 15 – 50 s for the majority bursts during the so-called cooling tails. In a subset of the cases, the luminosity reaches the Eddington luminosity where the radiation forces match or exceed the gravitational forces and lift the photosphere off of the neutron star surface. These photospheric radius expansion (PRE) events have characteristic signatures where the photosphere is observed to reach several times the neutron star radius and the temperature has a second rise (Lewin, van Paradijs & Taam 1993).

Several approaches have been developed and used to determine the neutron star radius by making use of thermonuclear bursts. van Paradijs (1979) introduced using the apparent angular size obtained during the cooling tails of the bursts as a way to obtain correlated M-R constraints. Subsequently, Fujimoto & Taam (1986), Sztajno et al. (1987), Damen et al. (1990), and Özel (2006) discussed different ways in which the degeneracy between the radius and the mass can be broken through multiple spectroscopic measurements.

Özel & Psaltis (2009), Güver et al. (2010a), and a number of studies since have used a combination of the apparent angular sizes, the Eddington fluxes obtained from the PRE bursts, and the source distances to measure the neutron star radius and mass. In particular, the apparent angular sizes were measured from the flux and the temperature obtained from time-resolved spectroscopy, while the Eddington limit is measured at the moment when the photosphere touches back down onto the stellar surface. The Eddington flux is related to stellar parameters M and R and distance D via

$$F_{\text{Edd}} = \frac{GMC}{k_{\text{es}}D^2} \left(1 - \frac{2GM}{Rc^2}\right)^{1/2}, \quad (11)$$

where

$$k_{\text{es}} \equiv 0.2(1 + X) \left[1 + \left(\frac{kT_c}{38.8 \text{ keV}}\right)^{a_g} \left(1 - \frac{2GM}{Rc^2}\right)^{-a_g/2}\right]^{-1} \text{ cm}^2 \text{ g}^{-1} \quad (12)$$

is the electron scattering opacity and the last term in the equation arises from temperature corrections to electron scattering (Paczynski 1983; Suleimanov, Poutanen & Werner 2012). X is the hydrogen mass fraction of the atmosphere,

$$a_g = 1.01 + 0.067 \left(\frac{g_{\text{eff}}}{10^{14} \text{ cm s}^{-2}}\right), \quad (13)$$

and the effective surface gravity is given by

$$g_{\text{eff}} = \frac{GM}{R^2} \left(1 - \frac{2GM}{Rc^2}\right)^{-1/2}. \quad (14)$$

Because the dependence of the Eddington flux on the stellar mass and radius (Eq. 11) is different from that of the apparent angular size (Eq. 10), combining these two spectroscopic measurements breaks the degeneracies between the stellar parameters introduced by general relativistic effects.

Atmosphere models during bursts are used for the interpretation of spectra and the correct measurement of effective temperatures. A number of such models have been developed, addressing the Comptonization of photons by the hot surface electrons with increasing levels

of sophistication, and have been calculated for a range of surface compositions and effective gravities (London, Taam & Howard 1986; Madej, Joss & Różańska 2004; Majczyna et al. 2005; Suleimanov, Poutanen & Werner 2012). The deviations from a blackbody at the effective temperature of the atmosphere are quantified by the so-called color correction factor $f_c = T_c/T_{\text{eff}}$, which is then folded into these measurements.

Finally, the measured angular sizes are subject to additional general relativistic corrections due to moderately high spin frequencies observed in neutron stars with thermonuclear bursts. In particular, the effects of the quadrupole moment and the ellipticity of the neutron star on the neutron-star spacetime as well as the rotational broadening of the thermal spectra can be calculated in the Hartle-Thorne metric and lead to corrections in the inferred angular size of the order of $\sim 10\%$ (Bauböck et al. 2015).

This approach has been applied to the neutron stars in the low-mass X-ray binaries EXO 1745–248 (Özel & Psaltis 2009), 4U 1820–30 (Güver et al. 2010a), 4U 1608–52 (Güver et al. 2010b), KS 1731–260 (Özel, Gould & Güver 2012), SAX J1748.9–2021 (Güver & Özel 2013), and 4U 1724–207 (Özel et al. 2015). Özel et al. (2015) performed an updated analysis using new statistical methods, the theoretical corrections discussed above, and uniformly incorporating systematic uncertainties into the measurements. The resulting 68% confidence contours over the mass and radius for these six neutron stars are shown in Fig 4. When combined, these measurements indicate neutron star radii in the 9.8 – 11 km range, which is consistent with the results obtained from the analyses of qLMXBs.

Another approach that has been utilized for radius measurements is to determine the spectral evolution of the color correction factor in PRE bursts (see Majczyna & Madej 2005; Suleimanov, Poutanen & Werner 2011; Poutanen et al. 2014). Because the spectral distortions depend on the effective surface gravity g_{eff} and the emitted flux, the change in the color correction factor with luminosity as the burst cools down from an Eddington flux can provide a measure of the stellar mass and radius. The application of this method to 4U 1728–34 (Majczyna et al. 2005), 4U 1724–207 (Suleimanov, Poutanen & Werner 2011) and 4U 1608–52 (Poutanen et al. 2014) led to radii measurements that range from being too small (in the case of 4U 1728–34) to being too large (4U 1608–52). As we will discuss later, these measurements are biased by the inherent limitations of the data. The data selection used in the latter studies will also be discussed below.

One final approach is to compare the observed properties of the bursts, such as their recurrence and decay times, and their peak fluxes, to the expectations from theoretical lightcurve models to infer a surface redshift for the neutron star. These constraints can then be combined with the spectral evolution during the burst cooling tails to obtain constraints on the neutron star radius. Unfortunately, the theoretical models in this case are not very predictive and fail to explain the lightcurves of nearly any of the nearly 50 sources extensively studied with RXTE (Heger et al. 2007; Galloway et al. 2008). Therefore, the application of this method has been limited to the one source, GS 1826–24, where models can approximately match the lightcurve properties, and resulted in the limits $R < 6.8 - 11.3$ km for $M < 1.2 - 1.7 M_{\odot}$ (Zamfir, Cumming & Galloway 2012), also consistent with the results obtained from qLMXBs and with PRE bursts (see Fig. 4).

As with the qLMXBs in globular clusters, several sources of systematic uncertainty exist in the spectroscopic measurements of thermonuclear bursts. Their effects on the radius measurements have been studied in recent years and will be discussed in some detail below.

Distances. Two of the three techniques discussed above rely on a measurement of source distances to obtain neutron star radii. For the sources that reside in globular clusters, the cluster distances are utilized. These are subject to the same uncertainties as those used for the qLMXB measurements. Other techniques have also been considered to measure distances to bursting neu-

tron stars (Kuulkers et al. 2003; Güver et al. 2010a; Özel, Gould & Güver 2012). In most cases, these measurement techniques either yield reliable lower limits or source distances with relatively large uncertainties, which dominate the resulting uncertainties in the radius measurements.

Detection of Outliers. As with all physical measurements, identification of outliers in datasets that may contaminate the results is an important issue. Güver, Özel & Psaltis (2012) and Güver, Psaltis & Özel (2012) developed a data-driven Bayesian Gaussian-mixture approach to identify the outliers in the spectroscopic burst data without any theoretical biases. The resulting selected data were used in the radius measurements reported in Özel et al. (2015). In an alternative approach, Poutanen et al. (2014) and Kajava et al. (2014) performed data selection by requiring that the observations follow theoretical expectations. This approach resulted in a selection of a different, and much smaller, subset of bursts and led to the measurement of a stellar radius $R > 12$ km for 4U 1608–52. The consistency of the burst evolution with theoretical expectations and the limitations of the latter method when applied to RXTE data are discussed in detail in Özel, Psaltis & Güver (2015).

3.2. Radii via Pulse Profile Modeling

Neutron star radii can also be measured or constrained by analyzing the properties of periodic brightness oscillations originating from temperature anisotropies on the surface of a spinning neutron star. The amplitudes and the spectra of the oscillation waveforms depend on the neutron-star spacetime, which determines the strength of the gravitational light bending the photons experience as they propagate to an observer at infinity (Pechenick, Ftaclas & Cohen 1983), as well as on the temperature profile on the stellar surface and on the beaming of the emerging radiation. Using theoretical models for the emerging radiation, the properties of the brightness oscillation can, therefore, be used to probe the stellar spacetime and to measure its radius and mass.

The theoretical work on neutron-star spacetimes has enabled increasingly more precise calculations of the effects of the gravitational lensing on the surface photons, which are used for the analyses of the waveforms. Earlier approximations appropriate for non-spinning neutron stars (Pechenick, Ftaclas & Cohen 1983) were supplemented by adding in the effects of Doppler shifts and aberration (Miller & Lamb 1998; Muno, Özel & Chakrabarty 2002; Poutanen & Beloborodov 2006) or those of frame dragging (Braja, Romani & Rauch 2000) for slow spins up to 300 Hz. At even faster spins, the oblateness of the neutron star and the quadrupole moment of its spacetime on the photon trajectories have been accurately accounted for (Morsink et al. 2007; Psaltis & Özel 2014). For stars near break-up (> 1 kHz), fully numerical solutions of the spacetimes become necessary (Cook, Shapiro & Teukolsky 1994; Stergioulas & Friedman 1995; Cadeau et al. 2007).

The waveforms depend also on the location and the size of the hotspots, the beaming pattern of the radiation emitted from the stellar surface, and the line of sight of the observer with respect to the rotation axis. Modeling the shapes and amplitudes of the waveforms, therefore, can yield constraints on a combination of all of these parameters and result in measurements of these parameters with correlated uncertainties. The challenge here is to reduce the number of unknowns and to eliminate the correlated uncertainties between the parameters in order to obtain a measurement of the neutron star radius. The size of the hotspot has a minor effect when it is sufficiently small (Bauböck et al. 2015)), so this parameter can be eliminated in some cases. The beaming of radiation can also be calculated from atmosphere models.

Analysis of the oscillation waveforms have been performed to explore the properties of numerous types of neutron stars. While this method yielded useful results on the surface emission properties of slow pulsars (Page 1995) and magnetars (DeDeo, Psaltis & Narayan 2001; Özel 2001), constraints

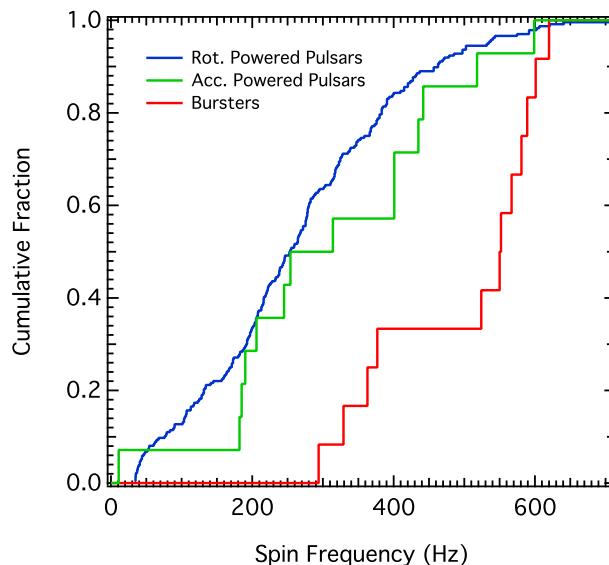


Figure 5

The cumulative distribution of spin frequencies of rotation-powered millisecond pulsars, accretion powered millisecond pulsars, and accreting neutron stars that show thermonuclear burst oscillations.

on the neutron-star radius and spacetime come, in particular, from the analysis of oscillations from accretion-powered millisecond pulsars, millisecond rotation-powered pulsars, and thermonuclear X-ray bursters. These last three classes have distributions of spin frequencies that differ from one another, as shown in Fig. 5. Therefore, spin effects need to be incorporated to different levels when modeling each population. We discuss the radius measurements from each of these classes individually below.

3.2.1. Rotation Powered Pulsars. Even though the emission from rotation-powered millisecond pulsars (MSPs) is largely non-thermal and is dominated by their magnetospheres, a number of sources show a clearly detected thermal component in the soft X-rays (e.g., Grindlay et al. 2002; Zavlin 2006, 2007; Bogdanov, Grindlay & Rybicki 2006). X-ray data from a number of MSPs, obtained with ROSAT, Chandra, and XMM-Newton, have been analyzed using hydrogen atmosphere models for the thermal emission from a polar cap (see, e.g., Zavlin & Pavlov 1998). In these models, pulse profiles are calculated based on the beaming of radiation predicted by the theoretical models (see Özel 2013 for details).

An analysis of PSR J0437–4715, assuming a mass of $1.4 M_{\odot}$ yielded bounds on the radius in the $R = 6.8 - 13.8$ km range (90% C.L.; Bogdanov, Rybicki & Grindlay 2007). A subsequent measurement of the pulsar mass at $1.76 M_{\odot}$ (Verbiest et al. 2008) increased the lower limit on the neutron star radius to $R > 11.1$ km (99.9% C.L.; see Fig. 6 and Bogdanov 2013), but this result is likely to be revised again in view of the most recent measurement of the pulsar mass (see Table 2). Similar analyses for pulsars J0030+0451 and J2124–3358 lead to lower limits on their radii of 10.7 km (95% C.L.) and 7.8 km (68% C.L.), respectively, assuming a pulsar mass of $1.4 M_{\odot}$.

There are a number of complexities that affect the interpretation of the pulsar waveform data from MSPs. First, the non-thermal magnetospheric emission is subtracted from the total observed emission in the X-rays to allow for a modeling of the thermal surface component from

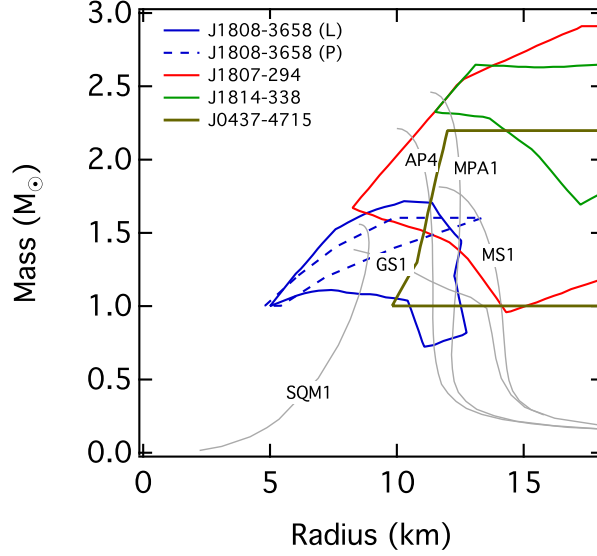


Figure 6

The radii constraints obtained from analysis of the waveforms from accretion-powered (Poutanen & Gierliński 2003; Leahy, Morsink & Cadeau 2008; Leahy et al. 2009; Leahy, Morsink & Chou 2011) and rotation-powered millisecond pulsars (Bogdanov 2013). Two different analyses of the SAX J1808.4-3658 data by Poutanen et al. (2003, denoted by P) and Leahy et al. (2008, denoted by L) are included.

the polar caps. The thermal component itself is typically modeled with two separate regions with different temperatures, each emitting with a hydrogen atmosphere spectrum (Zavlin 2006; Bogdanov, Rybicki & Grindlay 2007). The pulse profiles have been modeled with two polar caps but the waveforms have required a non-antipodal geometry and led to additional uncertainties from introducing an additional offset parameter. The footprints of polar caps in the studies performed to date have assumed circular caps but the effect of the shape of the polar cap on the waveforms have not yet been explored (see, however, Bauböck et al. 2015 for the effect of the unknown shape and size of the polar caps). Finally, the angles that specify the observer’s line-of-sight and the colatitude of the polar caps with respect to the stellar spin axis have been assumed to be known independently. The uncertainties introduced by the errors in these angles have not been factored into the quoted radius constraints. Future work is needed to assess the effects of these assumptions and to quantify the additional resulting uncertainties in the radius measurements.

3.2.2. Accretion Powered Pulsars. Thermal emission is observed in a number of accretion-powered millisecond X-ray pulsars (AMSPs) in the soft X-rays. It originates from the base of the accretion column, which is then Comptonized in that column (see section 3.3 of Poutanen & Gierliński 2003).

A number of studies have modeled the emission from the X-ray emitting regions at the bases of the accretion columns (Poutanen & Gierliński 2003; Lamb et al. 2009). The thermal photons emitted from the surface are Compton scattered in the accretion column, affecting the observed pulse amplitudes. Lamb et al. (2009) also explored the effect of the location of the X-ray emitting regions and considered models where the base of the accretion column wobble around the spin axes. These models help interpret the AMSP timing data but also explore uncertainties in the

mass-radius constraints obtained from fitting the waveforms.

This method has been applied to several accreting millisecond X-ray pulsars: SAX J1808.4–3658 (Poutanen & Gierliński 2003; Leahy, Morsink & Cadeau 2008; Morsink & Leahy 2011), XTE J1807–294 (Leahy, Morsink & Chou 2011), and XTE J1814–338 (Leahy et al. 2009). Fig. 6 shows the inferred constraints on the mass and radius of the neutron stars in these studies, where the contours depict 99% confidence levels. The large uncertainties in the mass-radius measurements shown in this figure reflect the influence of the various geometric factors discussed above, which are difficult to constrain.

3.2.3. Thermonuclear Burst Oscillations. Periodic flux oscillations with large amplitudes originating from the surfaces of neutron stars have also been detected during thermonuclear X-ray bursts (Strohmayer et al. 1996). They originate from temperature non-uniformities on the stellar surface that occur during the nuclear burning (see Watts 2012 for a review). Modeling the pulse profiles of these burst oscillations are also good probes of the stellar gravity and leads to constraints on the neutron star compactness (Strohmayer, Zhang & Swank 1997; Miller, Lamb & Psaltis 1998). In particular, the amplitude of the oscillations, the deviations from a sinusoidal waveform, and their dependence on photon energy can be probes of the neutron star radius and mass (Weinberg, Miller & Lamb 2001; Muno, Özel & Chakrabarty 2002, 2003).

This technique was applied to oscillations observed from 4U 1636–536 (Nath, Strohmayer & Swank 2002) but led to no significant constraints on the neutron star radius or compactness. For the neutron star in XTE J1814–338, the analysis of the waveforms of burst oscillations resulted in the limit on the neutron star compactness $R/M > 4.2$ (Bhattacharyya et al. 2005). Future observations can make use of more properties of the observed waveforms, such as their energy dependence and the amplitudes of the higher harmonics (Psaltis, Özel & Chakrabarty 2014), and the prospects are more comprehensively discussed in Watts et al. (2015).

4. The Neutron Star Equation of State

In addition to characterizing neutron star populations as well as understanding their formation and evolution, one of the ultimate goals of mass-radius measurements is, of course, to constrain the ultradense matter equation of state (EoS). The microphysics, as described by the EoS, is connected to the macroscopic properties of the neutron star via the Tolman-Oppenheimer-Volkoff equations, which provide the direct relation that is necessary to use astrophysical observations to constrain nuclear physics at very high densities. In this section, we will describe this relation, a variety of theoretical approaches to as well as the low-energy experimental constraints on the EoS, and the current measurement of the EoS beyond nuclear saturation density from neutron star observations.

4.1. Neutron Star Structure

The structure of relativistic stars and their mass-radius relation are determined by integrating the relativistic structure equations, also known as the Tolman-Oppenheimer-Volkoff (TOV) equations (Oppenheimer & Volkoff 1939; Tolman 1934, 1939)

$$\begin{aligned}\frac{dp}{dr} &= -\frac{G}{c^2} \frac{(p + \epsilon)(m + 4\pi r^3 p/c^2)}{r^2[1 - 2Gm/(rc^2)]} \\ \frac{dm}{dr} &= 4\pi r^2 \frac{\epsilon}{c^2},\end{aligned}\tag{15}$$

where p is the pressure, ϵ is the energy density, r is the radius, and m is the enclosed mass, from the center $r = 0$ where $p = p_c$ and $\epsilon = \epsilon_c$ to the surface at $r = R$, where $p = 0$ and the enclosed mass is equal to the total mass $m = M$. (At moderate spin frequencies $f_{\text{NS}} \lesssim 800$ Hz, rotational corrections appear at $< \text{few } \%$ level; see Cook, Shapiro & Teukolsky 1994; Stergioulas & Friedman 1995). To complete this set of equations, one needs to specify the pressure-energy density relation, referred to as the equation of state, appropriate for neutron-star matter.

Before we proceed with a discussion of the cold, dense matter EoS, a few remarks on the relevant quantities and units are in order. While the energy density ϵ enters the TOV equations, most nuclear EoS calculations also use or refer to the baryon number density n (in units of $\text{fm}^{-3} \equiv 10^{39} \text{cm}^{-3}$) or to the mass density ρ (in units of g cm^{-3}). The nuclear saturation density can then be equivalently expressed as a mass density $\simeq 2.8 \times 10^{14} \text{ g cm}^{-3}$ or a particle density $\simeq 0.16 \text{ fm}^{-3}$. Similarly, the pressure is typically expressed in units of $\text{MeV fm}^{-3} \equiv 1.6 \times 10^{33} \text{ dyne cm}^{-2}$.

In neutron star cores, matter is cold and ultradense, characterized by large chemical potentials and a significant asymmetry in the numbers of neutrons and protons. Indeed, the condition of β equilibrium, given by

$$\left(\frac{\partial \epsilon / n}{\partial Y_e} \right)_n = \mu_e + \mu_p - \mu_n = 0 \quad (16)$$

points to proton fractions of $x \lesssim 10\%$, unlike normal nuclei which possess nearly equal numbers of protons and neutrons (referred to as symmetric matter). In the equation above, ϵ/n is the energy per baryon, μ_e, μ_p , and μ_n are the chemical potentials of the electrons, protons, and neutrons, respectively, and Y_e is the number of electrons per baryon. The densities in the cores can reach $\sim 10\rho_{\text{sat}}$. Given that neutrons geometrically overlap at $\sim 4\rho_{\text{sat}}$, at these very high densities, matter may not be composed of nucleons alone but may contain a rich variety of hadronic degrees of freedom. With increasing overlap between nucleons, transitions to non-nucleonic states of matter are expected. For example, a gradual onset of quark degrees of freedom and quark constituents propagating throughout the system become likely (e.g., Alford et al. 2005a; Kojo et al. 2015). In addition, Bose-Einstein condensates of mesons, such as pion (Akmal, Pandharipande & Ravenhall 1998; Mukherjee 2009; Pandharipande, Pethick & Thorsson 1995) or kaon condensates (Kaplan & Nelson 1986; Brown et al. 1992; Glendenning & Schaffner-Bielich 1999) can enter at higher densities. It is also possible for ultradense matter to contain strange quarks in forms other than kaons, as weak interactions in the cold neutron-star cores can lead to states of matter with a high degree of strangeness. Some of the possibilities considered to date include the presence of hyperons (Ambartsumyan & Saakyan 1960; Glendenning & Moszkowski 1991; Schulze et al. 1995), hybrid stars containing free quarks (Collins & Perry 1975), or color superconducting phases (Alford & Reddy 2003; Alford et al. 2005b). Moreover, self-bound stars consisting of strange quark matter have also been proposed (Farhi & Jaffe 1984; Haensel, Zdunik & Schaefer 1986; Alcock, Farhi & Olinto 1986). These models are based on the assumption that strange quark matter is the ultimate ground state of matter (Witten 1984) and they predict stellar radii that grow with the stellar mass.

First principles QCD calculations are not yet able to describe the interactions of such a system at several times the nuclear saturation density (but there is significant recent progress in describing the quark matter EoS at even higher densities and extrapolating down to lower densities; see, e.g., the discussion and results in Kojo et al. 2015 and Kurkela et al. 2014). Because of that, a number of different approaches have been followed in the calculations of the equation of state of neutron star matter. A comprehensive overview of the methods and the details of the nuclear physics can be found in Glendenning (2000), Lattimer & Prakash (2001), and Baldo & Burgio (2012). Here, we provide a summary of the basic methods as well as a compilation of some representative model equations of state.

One common effective field theory motivated approach relies on expanding the nuclear Hamiltonians into two-, three-,... n -body static potential terms, assuming that the forces between particles can be described via static few-body potentials. The two-body potential is determined in the vicinity of ρ_{sat} for symmetric matter using nucleon-nucleon scattering data below 350 MeV and the properties of light nuclei, and the contributions from the three-body potentials are added (Akmal, Pandharipande & Ravenhall 1998; Morales, Pandharipande & Ravenhall 2002; Hebeler et al. 2010; Gandolfi, Carlson & Reddy 2012). The resulting equations of state are particularly sensitive to the three-nucleon interactions because of the near-cancellation between the kinetic term and the two-body term in these potentials. In addition, such expansions are not valid at $\rho \gg \rho_{\text{sat}}$ because the parameter measuring the relative importance of three and higher body forces is $\sim \rho/(2m_\pi)^3 \sim 0.35\rho/\rho_{\text{sat}}$.

In these approaches, it is also common to make use of nuclear Hamiltonians that are experimentally constrained for symmetric matter around nuclear density and express the energy per baryon at higher density and at higher neutron fraction as a parametric expansion in terms of the ratio $u \equiv \rho/\rho_{\text{sat}}$ and the neutron excess $1 - 2x$:

$$\frac{\epsilon(u, x)}{n} = -B + \frac{K_o}{18}(u-1)^2 + \frac{K'_o}{162}(u-1)^3 + S_2(u)(1-2x)^2 \quad (17)$$

In this expansion, $B \simeq 16$ MeV is the bulk binding energy of symmetric matter at nuclear saturation density and K_o and K'_o are the nuclear incompressibility and skewness parameters and we only show terms up to quadratic order. It is also customary to call the quadratic term in neutron excess the “symmetry energy” and express it in terms of two parameters S_v , the symmetry energy at nuclear density

$$S_v = S_2(1), \quad (18)$$

and L , which is related to the derivative of the symmetry energy with respect to density

$$L = 3u \left(\frac{dS_2}{du} \right)_{u=1}. \quad (19)$$

Naturally, at high density and high neutron fraction, these approaches also enter a regime where the expansions are not valid.

Alternatives to this approach include one that is based on field-theoretical calculations of constituents interacting via meson exchange (Müller & Serot 1996). A third approach involves microscopic ab initio calculations based on the Brueckner-Hartree-Fock model (Baldo, Bombaci & Burgio 1997) or its relativistic counterpart, the Dirac-Brueckner-Hartree-Fock model (Müther, Prakash & Ainsworth 1987), or its modifications using unconventional Skyrme forces (Goriely, Chamel & Pearson 2010; see also Potekhin et al. 2013 for analytical representations based on this equation of state).

Fig. 7 (left panel) shows a large sample of currently proposed equations of state, spanning a density range between $\sim 0.1 - 8\rho_{\text{sat}}$. The wide range of pressures P predicted under different assumptions are indicative of the wide open questions in physics in this regime. The acronyms and the references for the various equations of state can be found in Read et al. (2009). We also include in this figure (i) the recent equation of state labeled NJL (Kojo et al. 2015) based on a smooth interpolation in pressure vs. baryon chemical potential of a nucleonic equation of state (APR) at densities below $\sim \rho_{\text{sat}}$ with a quark matter equation of state at densities above $\sim 5 - 7\rho_{\text{sat}}$, (ii) the BSK equation of state of Goriely, Chamel & Pearson (2010) and Potekhin et al. (2013), and (iii) the QMC equation of state of Rikowska Stone et al. (2007).

The mass-radius relations corresponding to the equations of state in Fig. 7 are shown in the right panel. The curves that do not reach the observed $\sim 2 M_\odot$ mass limit are denoted in light grey in

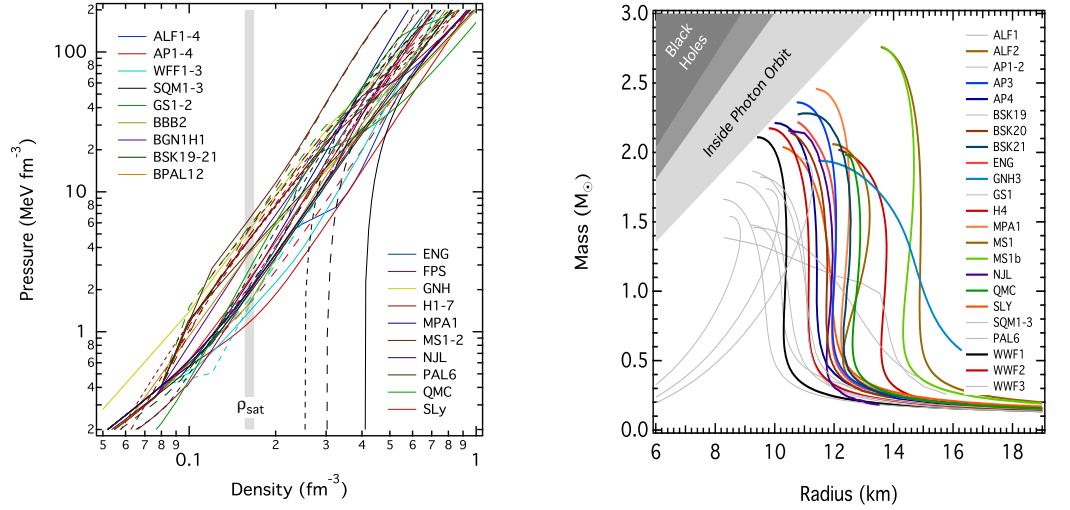


Figure 7

(Left) A large sample of proposed equations of state calculated under different physical assumptions and using a range of computational approaches. See the text for the descriptions of the equations of state, the acronyms, and the references. (Right) The mass-radius curves corresponding to the equations of state shown in the left panel.

this figure. Also note that the astrophysically relevant parts of these curves lie above $\sim 1 M_{\odot}$. An important characteristic of many of these curves is that the radius remains nearly constant for the astrophysically relevant range of masses. The notable exceptions are the self-bound strange stars (e.g., SQM), where the radius increases with increasing mass, and stars with condensates (e.g., GS1-2, GM, PS) where the radius decreases with mass past the point where the central density reaches the critical one where the phase transition occurs. The mass-radius curves are also characterized by a maximum mass beyond which there are no stable solutions. In general, equations of state with relatively higher pressures at densities above $\sim 4 \rho_{\text{sat}}$ have higher maximum masses. The presence of non-nucleonic phases, such as hyperons or condensates, reduces the pressure (referred to as softening the equation of state) lead to smaller maximum masses.

In the remainder of this section, we will discuss how neutron star masses and radii can be used to pin down the ultradense matter equation of state, the methodologies developed towards this goal, and the current state of the measurements. However, we first briefly describe the constraints on the nuclear EoS at nuclear density from low energy experiments.

4.2. Constraints on the EoS from Low Energy Experiments

For symmetric matter (i.e., nuclei containing roughly equal number of neutrons and protons) near the nuclear saturation density, there is a range of experimental constraints. Most robustly, two-body potentials can be inferred from nucleon-nucleon scattering data below 350 MeV and the properties of light nuclei (Akmal, Pandharipande & Ravenhall 1998; Morales, Pandharipande & Ravenhall 2002).

The other significant constraints that arise from these experiments and are relevant for the neutron-star equation of state are often expressed in terms of the symmetry energy parameters: S_v and L (see eq'ns 18 and 19 in the previous section as well as the discussion in Lattimer 2012). The experiments that yield the most accurate data and the least model-dependent results involve

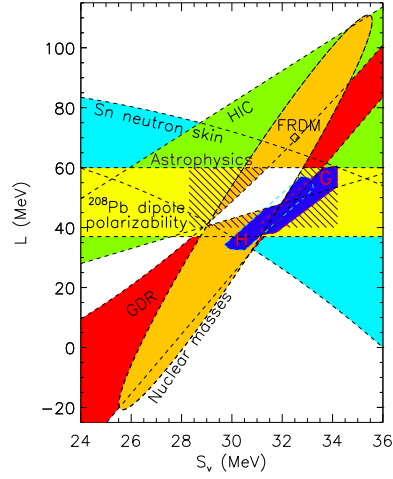


Figure 8

The experimental constraints on the symmetry energy parameters L and S_v from experiments performed near nuclear density. These include the neutron skin thickness of neutron-rich Sn isotopes (shown in blue), giant dipole resonances (red), the dipole polarizability of ^{208}Pb (light yellow), heavy-ion collisions (green), as well as nuclear masses (dark yellow). The theoretical inferences from Gandolfi (2012, G) and Hebeler (2010, H), as well as an earlier astrophysical inference from Lattimer 2012 are also indicated on this figure as dark blue and hatched regions, respectively. Reproduced with permission from Lattimer 2012.

fitting nuclear masses and charge radii (Klüpfel et al. 2009; Kortelainen et al. 2010). Nevertheless, the symmetry parameters that can be extracted from such data are highly correlated, as shown in Fig. 8.

Neutron-rich matter can also be probed by measuring the neutron skin thickness of heavy nuclei. Studies within both the mean-field theory and the liquid droplet model frameworks have shown that the neutron skin thickness, defined as the difference of their neutron and proton root-mean-squared radii

$$\Delta r_{np} = \langle r_n^2 \rangle^{1/2} - \langle r_p^2 \rangle^{1/2} \quad (20)$$

is a sensitive function of S_v and L and, thus, serves as a good probe of the symmetry energy (Centelles et al. 2009; Chen et al. 2010; Roca-Maza et al. 2011). The neutron skin thickness was measured by a variety of experiments for ≈ 20 neutron-rich Sn isotopes with $\sim 30 - 50\%$ uncertainties. Chen et al. (2010) used these measurements to place additional constraints on the symmetry energy parameters (see Fig. 8). In addition, the neutron skin thickness has been determined by the PREX experiment for ^{208}Pb using a technique called parity-violating electron scattering (Abrahamyan et al. 2012): because the weak-vector meson that mediates this interaction couples preferentially to neutrons, the approach allows a measurement of the neutron form factor, which can then be extrapolated to neutron skin thickness.

Another observable that places significant constraints on L come from the measurement of the dipole polarizability of ^{208}Pb and the giant dipole resonances. The giant dipole resonance, measured from the response of the neutron-rich nuclei to an externally applied electric field, serves as a measure of the symmetry energy (Trippa, Colò & Vigezzi 2008; Tamii et al. 2011; Piekarewicz et al.

2012). The resulting constraints on S_v and L are also shown in Fig. 8.

The most indirect experimental probe of the EoS of cold, neutron-rich, dense matter emerge from low-energy heavy-ion collisions. There are large uncertainties in extrapolating from the properties of hot dense matter generated in these collisions to zero temperature and to extreme neutron-richness (Tsang et al. 2009). For completeness, Fig. 8 also includes these constraints.

While none of these experiments are as powerful and direct probes of the neutron star EoS as the measurement of the macroscopic properties of neutron stars (as will be shown in the next section), they serve as complementary tests of the properties of dense matter. At a minimum, the pressure obtained from the two-nucleon interaction serves as a lower limit to the pressure of neutron-star matter at $\sim 1 - 2 \rho_{\text{sat}}$. This is because three-body interactions in pure neutron matter are always repulsive. Considering the expansion of the interaction in terms of two- and three-body potentials and using the contribution of the two-body potential (Argonne AV8 or AV18) yields a lower bound of $P = 7.56 \text{ MeV fm}^{-3}$ at $\rho = 1.85 \rho_{\text{sat}}$ (Özel et al. 2015). This constraint has been used in conjunction with the neutron star radius measurements to determine the ultradense matter EoS, as we will discuss in Section 4.4.

4.3. From Radius and Mass Measurements to the Neutron Star EoS

Given the Tolman-Oppenheimer-Volkoff equations, the EoS of neutron star matter determines the macroscopic properties of the stars and, in particular, their masses and radii. In fact, the solutions provide a unique map between the microscopic pressure-density relation ($P(\rho)$ or $P(\epsilon)$) and the macroscopic mass-radius relation of stars (Lindblom 1992).

This unique mapping can, in principle be exploited to infer the EoS from astrophysical measurements of their masses and radii. However, a formal inversion of this mapping requires a measurement of the entire mass-radius curve, i.e., the measurement of radii for neutron stars that span the range of stellar masses between $\sim 0.2 - 2M_{\odot}$. This requirement severely limits the applicability of this direct inversion because there is no astrophysical formation channel for neutron stars with masses that are much smaller than the Chandrasekhar mass of the progenitor cores and neither are such stars observed (see Section 2).

Despite this difficulty, the connection between the mass-radius relations and the EoS turn out to have certain characteristics that make it possible to infer them from a more sparse sampling of neutron star radii. In particular, the maximum mass is determined primarily by the behavior of the equation of state at the highest densities ($\sim 7 - 8 \rho_{\text{sat}}$; Özel & Psaltis 2009), while the radius depends primarily on the pressure at $\approx 2 \rho_{\text{sat}}$ (Lattimer & Prakash 2001). The slope of the mass-radius relation (i.e., whether R increases or decreases with M), in the mass range of astrophysical interest, depends largely on the pressure at $\sim 4 \rho_{\text{sat}}$ (Özel & Psaltis 2009). The fact that only a small number of densities determines the macroscopic properties of neutron stars means that their various higher order moments cannot be completely independent from each other. Indeed, a number of universal relations have been found between various higher-order moments of neutron stars (Yagi & Yunes 2013; Bauböck et al. 2013; Yagi et al. 2014), the origins of which have not yet been fully understood.

These properties make it possible to infer the pressure of ultradense matter at a few appropriately chosen densities above ρ_{sat} instead of mapping out the full functional form of the EoS from astrophysical observations. The optimal densities for sampling and the parametric forms that lead to the smallest uncertainties in the EoS determination were explored in detail by Read et al. (2009) and Özel & Psaltis (2009). These studies showed that the pressures measured at $1.85 (P_1)$, $3.7 (P_2)$, and $7.4 \rho_{\text{sat}} (P_3)$ and connected by piecewise polynomials can represent more than forty proposed EoS included in those studies to within few percent uncertainty. These led to the real-

ization that the measurement of the masses and radii of even a small number of neutron stars can provide significant input to the microphysics calculations, which was used in the subsequent studies (Özel, Baym & Güver 2010; Steiner, Lattimer & Brown 2010; Guillot & Rutledge 2014).

The mass of the heaviest neutron star measured to date can provide additional direct constraints on the EoS. At a minimum, the EoS that have maximum masses that fall below the the most massive neutron star can be ruled out (Demorest et al. 2010; Özel et al. 2010; Antoniadis et al. 2013). However, more stringent constraints are achieved by combining the floor on the maximum mass with radius measurements (Steiner, Lattimer & Brown 2010; Özel et al. 2015). Because the EoS that produce smaller radii generally tend to have smaller maximum masses, combining these measurements yield smaller allowed confidence regions in the EoS parameters.

Bayesian techniques have been developed (Steiner, Lattimer & Brown 2010, 2013; Özel et al. 2015) to combine radius measurements, the maximum mass constraint, as well as the data obtained from the low-energy experiments discussed in the previous section. These techniques yield likelihoods over the EoS parameters P_1, P_2 and P_3 from the mass-radius likelihoods $P(M_i, R_i)$ for i sources, while allowing a variety of priors and other measurements to be incorporated (see Özel et al. 2015 and references therein for details).

The priors over P_1, P_2 , and P_3 are then specified using numerous physical and observational constraints. First, for the EoS to be microscopically stable, it is necessary to require $P_3 \geq P_2 \geq P_1$, and that P_1 be greater than or equal to the pressure of matter at $\rho_0 = 10^{14} \text{ g cm}^{-3}$ (see Özel & Psaltis 2009 for the particular specification using the SLy EoS). Second, for the EoS to be causal, the condition

$$c_s^2 = \frac{\partial P}{\partial \epsilon} \leq c^2, \quad (21)$$

where, c_s is the sound speed and ϵ is the energy density, can be imposed at all densities. Third, to incorporate the mass requirement, the maximum stable mass for each EoS corresponding to a P_1, P_2, P_3 triplet needs to exceed $1.97M_\odot$, consistent within 1σ with the heaviest neutron stars observed to date.

The results from the laboratory experiments can be folded in as a requirement on the pressure at the lowest density P_1 or as constraints on the symmetry energy parameters L and S_v , which can be translated into constraints on P_i . As discussed in Section 4.2, the least model-dependent one of those requirements is a lower limit on $P_1 = 7.56 \text{ MeV fm}^{-3}$ such that the EoS is consistent with the most robust laboratory experiments and low density calculations, i.e., with the APR EoS for pure neutron matter (Akmal, Pandharipande & Ravenhall 1998). Finally, priors that are flat in $\log P_1$, $\log P_2$, and $\log P_3$ or that are flat in P_1 , P_2 , and P_3 can be chosen. The sensitivity of the Bayesian inference of the EoS parameters on these conditions and priors is discussed in Steiner, Lattimer & Brown (2013) and Özel et al. (2015).

4.4. Current constraints on the cold neutron matter EoS

In recent studies, the radius results summarized in Section 3 have been used in conjunction with the Bayesian parameter inference techniques to place strong constraints on the neutron star EoS. The radius data include the fourteen sources shown in Figure 4. (Note that these omit the analysis of 4U 1724–207 by Suleimanov, Poutanen & Werner 2011 and 4U 1608–52 by Poutanen et al. 2014, for which the data selection and analysis do not yield self-consistent results.)

Figure 9 shows the posterior likelihoods over the pressures at the three fiducial densities, as well as the microscopic and experimental bounds on these pressures. The pressures at the fiducial densities of a large number of proposed EoS are also shown. The gray region labeled 2NI denotes the lower limit on P_1 coming from the two-body interaction potential obtained at low densities. P_1 is also constrained from above by the the relatively small measured radii. Indeed, the values within

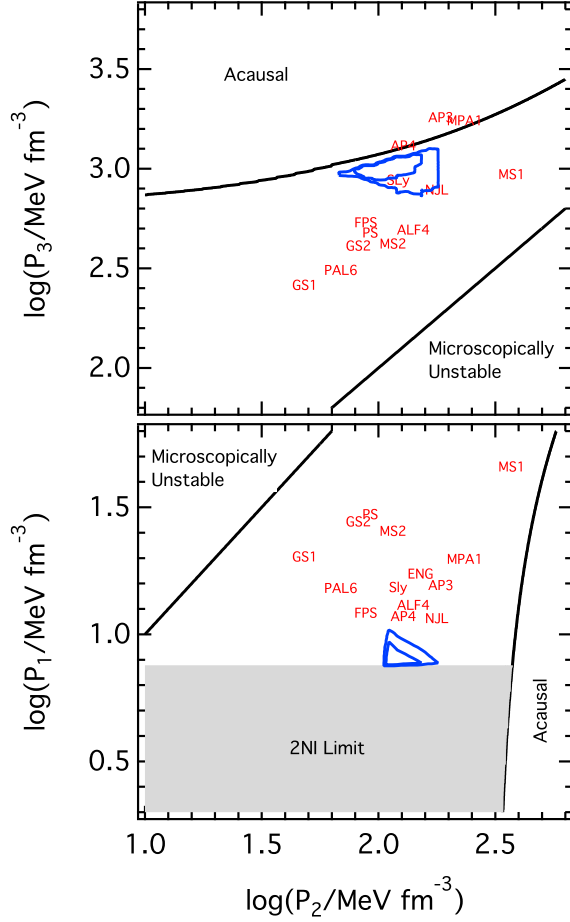


Figure 9

The highest likelihood regions in the pressure of neutron star matter at $1.85 \rho_{\text{ns}}$ (P_1), $3.7 \rho_{\text{ns}}$ (P_2), and $7.4 \rho_{\text{ns}}$ (P_3) obtained by a parametric inversion of all the neutron star radius measurements and requiring that it is consistent with the maximum mass requirement and low-energy experiment data. To visualize the structure of the three-dimensional posterior likelihood function, the contours outline the regions in which the posterior likelihoods drop down to $e^{-1/2}$ and e^{-1} of the highest value. The allowed regions of the parameter space are consistent with the constraints from calculations based on low-energy scattering experiments, are microscopically stable, and ensure that the EoS remains causal.

the highest posterior likelihood is lower than the pressure predicted by most proposed EoS at that density.

The combination of P_2 and P_3 , on the other hand, is constrained by the maximum mass requirement: a lower value of P_2 pushes P_3 to be as high as possible within the causality limit, whereas for moderate to high values of P_2 , which already lead to M-R relations that allow high mass stars and are consistent with the radius measurements, the allowed range of P_3 extends to lower values. The combination of P_2 and P_3 exclude to high confidence the stiff EoS such as MPA1 and MS1, which produce radii that are too large (see also their inconsistency with P_1 in the lower panel). This combination also excludes EoS with condensates, such as GS1, with pressures that are too low

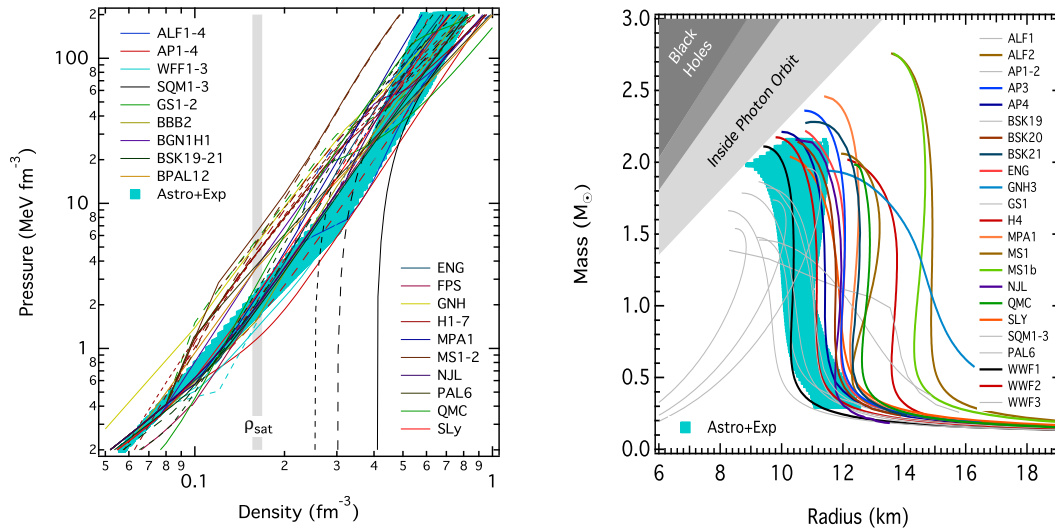


Figure 10

The astrophysically inferred (left) EoS and (right) mass-radius relation corresponding to the most likely triplets of pressures that agree with all of the neutron star radius and low energy nucleon-nucleon scattering data and allow for a $M > 1.97 M_{\odot}$ neutron star mass. The light blue bands show the range of pressures and the mass-radius relations that correspond to the region of the (P_1, P_2, P_3) parameter space in which the likelihood is within e^{-1} of its highest value. Around $1.5 M_{\odot}$, this inferred EoS predicts radii between $9.9 - 11.2$ km.

to be consistent with the maximum mass requirement.

Figure 9 shows that the combination of the radius measurements with the low density experimental data and the requirement of a $\sim 2 M_{\odot}$ maximum mass pins down the parameters of the EoS extremely well across a wide range of supranuclear densities and points to a preferred EoS that is somewhat softer than the nuclear EoS AP4 (a version of the APR EoS). To see this on the mass-radius diagram, we also show in Figure 10 the mass-radius relation corresponding to the most likely triplet of pressures as well as the range of mass-radius relations for the region of the (P_1, P_2, P_3) parameter space with the highest likelihood. We limit the range of masses in this figure to $\leq 2.2 M_{\odot}$ because of the absence of any data to constrain the relation at higher masses. As expected from the above discussion, the preferred mass-radius relation lies to the left of most model predictions and is closest to AP4, especially at low masses, where the main uncertainty in AP4 is in the strength of the three-nucleon interactions. It also rises along a nearly constant radius in order to reach the $\sim 2 M_{\odot}$ limit. Depending on the choice of the prior, the predicted radius for a $1.5 M_{\odot}$ neutron star is between 9.9 and 11.2 km.

5. Future Prospects

5.1. The future of radio pulsar mass measurements: New surveys, new binary systems, new measurements - and the SKA

We can expect the number of mass measurements to increase at an accelerating rate over the next few years. The reason for this is that improvements in instrumentation, both in terms of new receivers and the equipment used to detect and process the radio signals, are revolutionizing the field of pulsar timing and searching.

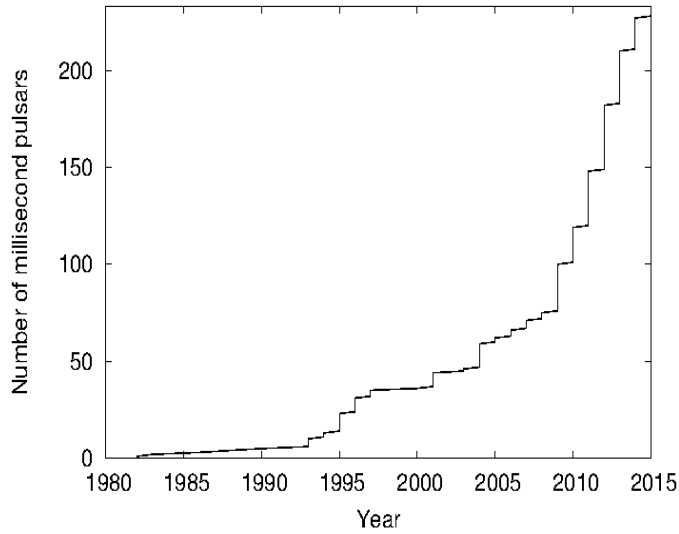


Figure 11

Number of MSPs (with $P < 20$ ms) known in the Galactic disk as a function of time. This figure does not take into account the more than 100 MSPs known in globular clusters. The large number of discoveries in recent years was enabled by improvements in the digital equipment being used in ground-based radio surveys and the discovery of many pulsar-like gamma-ray point sources by the Fermi satellite, which led to the discovery of many new radio MSPs. Data provided by Duncan Lorimer, see <http://astro.phys.wvu.edu/GalacticMSPs/GalacticMSPs.txt>.

More sensitive receivers with larger bandwidths and the advent of broadband coherent dedispersion allow much more precise timing of the known binary pulsars. This leads to more precise measurements of known PK parameters and the detection of new ones, greatly increasing the sample of NS mass measurements and the number of GR tests in different systems. Furthermore, improved receiver sensitivities and larger bandwidth, together with multi-beaming, increase the general sensitivity to all sorts of pulsars, as in the case of the phenomenally successful Parkes multibeam (PMB) surveys (Manchester et al. 2001). Since then, the newer generation of post-PMB surveys like the new HTRU-South (Keith et al. 2010) and North surveys (Barr et al. 2013), the Green Bank drift scan survey (Boyles et al. 2013; Lynch et al. 2013), the Green Bank North Celestial Cap survey (Stovall et al. 2014), the Arecibo ALFA survey (Cordes et al. 2006; Lazarus 2013) and the Arecibo 327 MHz drift-scan survey (Deneva et al. 2013) has been making full use of much improved data handling capabilities and processing power to obtain a large increase in spectral and time resolution (at a cost of 100 times the data rate). This has paid off with a great increase in the sensitivity to millisecond pulsars, particularly the distant ones, with a great leap in their discovery rate. The number of discoveries per year is shown in Fig. 11; we see a 3-fold increase in the number of MSPs since 2010. This will continue for the next few years, as many of the new surveys are still starting. The rate of discovery will further accelerate as soon as Square Kilometer Array (SKA) comes online (Kramer & Stappers 2015).

Not all these new MSPs were found in blind surveys. More than 100 were discovered in targeted

radio searches of globular clusters⁵. This number is expected to increase to thousands with the SKA (Hessels et al. 2015). A new and very successful search strategy – with more than 60 new MSPs discovered at the time of writing – has been targeting unidentified pulsar-like gamma-ray sources discovered with the *Fermi* satellite (see, e.g., Ransom et al. 2011; Keith et al. 2011; Kerr et al. 2012). Apart from the intrinsic interest in discovering new MSPs, the gamma-ray pulsars are important in the sense that they are biased *in favor* of very short-period MSPs, which is the opposite of the outcome in normal blind surveys. This contributes to a better understanding of the underlying MSP population.

The large increase in the number of binary pulsars implies a large increase in the number of NS mass measurements and tests of GR, because discoveries of more edge-on systems will inevitably result from a larger MSP sample, as well as discoveries of more triples, eccentric MSP systems, and DNSs. This trend is evident in Tables 1 and 2, where most of the reported results are relatively recent. Furthermore, the large sensitivity of planned radio telescopes such as the SKA will enable much improved timing precision of binary pulsars, new and old. This will further increase the number and precision of neutron star mass measurements and possibly allow a measurement of the upper mass limit for neutron stars.

5.2. The Future of Radius Measurements

The increase in the number of neutron star radius measurements and the continued reduction of the uncertainties will rely on a few factors. Distance uncertainties are currently one of the bottlenecks in the spectroscopic radius measurements. Therefore, one of the crucial improvements in this technique can come from obtaining distance measurements to many more neutron star X-ray binaries. The GAIA mission and radio parallax measurements may provide distances to the ones that are relatively nearby.

Radius measurements obtained by non-spectroscopic techniques, with potential biases and systematic uncertainties that are different than the spectroscopic ones will be another key factor in verifying the current measurements. To this end, high signal-to-noise pulse profiles of rotation- and accretion-powered X-ray pulsars will provide a major step forward. Indeed, the technique of pulse profile modeling to measure the neutron star compactness and radii defines the key scientific objectives of several future X-ray missions, such as NASA’s upcoming NICER (Gendreau, Arzoumanian & Okajima 2012), ISRO’s *Astrosat* (Agrawal 2006) or the proposed LOFT (Feroci et al. 2012) missions.

Among these missions, NICER, a NASA Mission of Opportunity, is poised to be launched to the International Space Station in 2016. NICER will collect a large number of counts from a small number of rotation-powered pulsars that emit thermally from their polar caps. In combination with the refined theoretical models that have been developed to analyze these waveforms, these data will provide a new measurement of neutron star radii and equation of state.

5.3. Other Future Probes of Neutron Star Structure

The double pulsar will be the first system that will allow, in a few years, a measurement of the moment of inertia of a neutron star (Lyne et al. 2004). The moment of inertia, being a higher moment of the mass distribution of the neutron star, is a powerful probe of its internal structure and, hence, of its equation of state (Morrison et al. 2004; Lattimer & Schutz 2005).

There are also significant prospects for radius measurements from Advanced LIGO observations

⁵See <http://www.naic.edu/~pfreire/GCpsr.html>

of coalescing neutron star binaries. The characteristic frequencies of these waveforms can be used to obtain information on the neutron star radius and deformability (see, e.g., Read et al. 2013), which will shrink the current uncertainties in the radius measurements and further constrain the dense matter equation of state.

Finally, the equation of state of neutron stars can be inferred by measuring the total luminosity and the spectrum of neutrinos emitted during a core-collapse supernova explosion within our Galaxy.

FUTURE ISSUES

1. Continued measurements of neutron star masses will make the inferred neutron star mass distributions more robust and help constrain the maximum neutron star mass by increasing the size of the sample.
2. Comparing current radius measurements against those made with other techniques will further reduce the uncertainties in the neutron star radii.
3. Multi-messenger probes such as gravitational waves, neutrinos, and moment-of-inertia measurements will open new avenues into neutron star structure.
4. Advances in lattice QCD will provide a first-principles calculation of the composition and interactions of the dense matter equation of state, which can be compared with the results from neutron stars and laboratory experiments.
5. The hot dense matter equation of state that is relevant to supernovae and neutron star mergers requires further study.

DISCLOSURE STATEMENT

The authors are not aware of any affiliations, memberships, funding, or financial holdings that might be perceived as affecting the objectivity of this review.

ACKNOWLEDGMENTS

We thank John Antoniadis, Ben Lackey, Jim Lattimer, Michael Kramer, Duncan Lorimer, Dimitrios Psaltis, Jocelyn Read, and Mallory Roberts for graciously providing materials for this review. We thank Gordon Baym, Tolga Güver, Ramesh Narayan, and Dimitrios Psaltis for numerous useful conversations and comments on the manuscript. F.Ö. gratefully acknowledges support from NSF grant AST 1108753. P.C.C.F. gratefully acknowledges financial support by the European Research Council for the ERC Starting grant BEACON under contract No. 279702.

LITERATURE CITED

- Abdo AA, Ajello M, Allafort A, Baldini L, Ballet J, et al. 2013. ApJS 208:17
- Abrahamyan S, Ahmed Z, Albataineh H, Aniol K, Armstrong DS, et al. 2012. *Physical Review Letters* 108:112502
- Agrawal PC. 2006. *Advances in Space Research* 38:2989–2994
- Akmal A, Pandharipande VR, Ravenhall DG. 1998. Phys. Rev. C 58:1804–1828
- Alcock C, Farhi E, Olinto A. 1986. ApJ 310:261–272
- Alford M, Braby M, Paris M, Reddy S. 2005a. ApJ 629:969–978
- Alford M, Braby M, Paris M, Reddy S. 2005b. ApJ 629:969–978
- Alford M, Reddy S. 2003. Phys. Rev. D 67:074024
- Ambartsumyan VA, Saakyan GS. 1960. AZh 37:193

- Antoniadis J, Bassa CG, Wex N, Kramer M, Napiwotzki R. 2011. MNRAS 412:580–584
- Antoniadis J, Freire PCC, Wex N, Tauris TM, Lynch RS, et al. 2013. *Science* 340:448
- Antoniadis J, Tauris T, Özel F, Freire P, Kramer M. 2016. ApJ In preparation
- Antoniadis J, van Kerkwijk MH, Koester D, Freire PCC, Wex N, et al. 2012. MNRAS 423:3316–3327
- Arzoumanian Z, Brazier A, Burke-Spolaor S, Chamberlin S, Chatterjee S, et al. 2015. ApJ 813:65
- Backer DC, Kulkarni SR, Heiles C, Davis MM, Goss WM. 1982. Nature 300:615–618
- Bailes M. 2010. New A Rev. 54:80–86
- Baiotti L, Giacomazzo B, Rezzolla L. 2008. Phys. Rev. D 78:084033
- Baldo M, Bombaci I, Burgio GF. 1997. A&A 328:274–282
- Baldo M, Burgio GF. 2012. *Reports on Progress in Physics* 75:026301
- Barr ED, Champion DJ, Kramer M, Eatough RP, Freire PCC, et al. 2013. MNRAS 435:2234–2245
- Barr ED, Freire PCC, Kramer M, Champion D. 2016. MNRAS In preparation
- Bassa CG, van Kerkwijk MH, Koester D, Verbunt F. 2006. A&A 456:295–304
- Bauböck M, Berti E, Psaltis D, Özel F. 2013. ApJ 777:68
- Bauböck M, Özel F, Psaltis D, Morsink SM. 2015. ApJ 799:22
- Bauswein A, Janka HT, Hebeler K, Schwenk A. 2012. Phys. Rev. D 86:063001
- Bégin S. 2006. A Search for Fast Pulsars in Globular Clusters
- Bhat NDR, Bailes M, Verbiest JPW. 2008. Phys. Rev. D 77:124017
- Bhattacharyya S, Strohmayer TE, Miller MC, Markwardt CB. 2005. ApJ 619:483–491
- Bogdanov S. 2013. ApJ 762:96
- Bogdanov S, Grindlay JE, Rybicki GB. 2006. ApJ 648:L55–L58
- Bogdanov S, Heinke CO, Özel F, Güver T. 2016. *ArXiv e-prints*
- Bogdanov S, Rybicki GB, Grindlay JE. 2007. ApJ 670:668–676
- Boyles J, Lynch RS, Ransom SM, Stairs IH, Lorimer DR, et al. 2013. ApJ 763:80
- Braje TM, Romani RW, Rauch KP. 2000. ApJ 531:447–452
- Brown EF, Bildsten L, Chang P. 2002. ApJ 574:920–929
- Brown EF, Bildsten L, Rutledge RE. 1998. ApJ 504:L95–L98
- Brown GE, Kubodera K, Rho M, Thorsson V. 1992. *Physics Letters B* 291:355–362
- Cadeau C, Morsink SM, Leahy D, Campbell SS. 2007. ApJ 654:458–469
- Callanan PJ, Garnavich PM, Koester D. 1998. MNRAS 298:207–211
- Camilo F, Kerr M, Ray PS, Ransom SM, Sarkissian J, et al. 2015. ApJ 810:85
- Caraveo PA. 2014. ARA&A 52:211–250
- Centelles M, Roca-Maza X, Viñas X, Warda M. 2009. *Physical Review Letters* 102:122502
- Champion DJ, Lorimer DR, McLaughlin MA, Xilouris KM, Arzoumanian Z, et al. 2005. MNRAS 363:929–936
- Champion DJ, Ransom SM, Lazarus P, Camilo F, Bassa C, et al. 2008. *Science* 320:1309–
- Chen LW, Ko CM, Li BA, Xu J. 2010. Phys. Rev. C 82:024321
- Cocozza G, Ferraro FR, Possenti A, D’Amico N. 2006. ApJ 641:L129–L132
- Collins JC, Perry MJ. 1975. *Physical Review Letters* 34:1353–1356
- Cook GB, Shapiro SL, Teukolsky SA. 1994. ApJ 424:823–845
- Cordes JM, Freire PCC, Lorimer DR, Camilo F, Champion DJ, et al. 2006. ApJ 637:446–455
- Corongiu A, Kramer M, Stappers BW, Lyne AG, Jessner A, et al. 2007. A&A 462:703–709
- Damen E, Magnier E, Lewin WHG, Tan J, Penninx W, van Paradijs J. 1990. A&A 237:103–109
- Damour T. 2015. *Classical and Quantum Gravity* 32:124009
- Damour T, Deruelle N. 1985. *Ann. Inst. Henri Poincaré Phys. Théor., Vol. 43, No. 1, p. 107 - 132* 43:107–132
- Damour T, Deruelle N. 1986. *Ann. Inst. Henri Poincaré Phys. Théor., Vol. 44, No. 3, p. 263 - 292* 44:263–292
- Damour T, Esposito-Farèse G. 1996. Phys. Rev. D 54:1474–1491
- DeDeo S, Psaltis D, Narayan R. 2001. ApJ 559:346–352
- Demorest PB, Pennucci T, Ransom SM, Roberts MSE, Hessels JWT. 2010. Nature 467:1081–1083
- Deneva JS, Stovall K, McLaughlin MA, Bates SD, Freire PCC, et al. 2013. ApJ 775:51

- Desvignes G, Caballero RN, Lentati L, Verbiest JPW, Champion DJ, et al. 2016. *ArXiv e-prints*
- Edwards RT, Bailes M. 2001. *ApJ* 553:801–808
- Falanga M, Bozzo E, Lutovinov A, Bonnet-Bidaud JM, Fetisova Y, Puls J. 2015. *A&A* 577:A130
- Farhi E, Jaffe RL. 1984. *Phys. Rev. D* 30:2379–2390
- Ferdman RD, Stairs IH, Kramer M, Janssen GH, Bassa CG, et al. 2014. *MNRAS* 443:2183–2196
- Ferdman RD, Stairs IH, Kramer M, McLaughlin MA, Lorimer DR, et al. 2010. *ApJ* 711:764–771
- Feroci M, Stella L, van der Klis M, Courvoisier TJL, Hernanz M, et al. 2012. *Experimental Astronomy* 34:415–444
- Fonseca E, Pennucci TT, Ellis JA, Stairs IH, Nice DJ, et al. 2016. *ArXiv e-prints*
- Fonseca E, Stairs IH, Thorsett SE. 2014. *ApJ* 787:82
- Freire PC, Camilo F, Kramer M, Lorimer DR, Lyne AG, et al. 2003. *MNRAS* 340:1359–1374
- Freire PCC, Bassa CG, Wex N, Stairs IH, Champion DJ, et al. 2011. *MNRAS* 412:2763–2780
- Freire PCC, Ransom SM, Bégin S, Stairs IH, Hessels JWT, et al. 2008a. *ApJ* 675:670–682
- Freire PCC, Ransom SM, Gupta Y. 2007. *ApJ* 662:1177–1182
- Freire PCC, Wex N. 2010. *MNRAS* 409:199–212
- Freire PCC, Wex N, Esposito-Farèse G, Verbiest JPW, Bailes M, et al. 2012. *MNRAS* 423:3328–3343
- Freire PCC, Wolszczan A, van den Berg M, Hessels JWT. 2008b. *ApJ* 679:1433–1442
- Fujimoto MY, Taam RE. 1986. *ApJ* 305:246–250
- Galloway DK, Muno MP, Hartman JM, Psaltis D, Chakrabarty D. 2008. *ApJS* 179:360–422
- Gandolfi S, Carlson J, Reddy S. 2012. *Phys. Rev. C* 85:032801
- Gendreau KC, Arzoumanian Z, Okajima T. 2012. In *Society of Photo-Optical Instrumentation Engineers (SPIE) Conference Series*, vol. 8443 of *Society of Photo-Optical Instrumentation Engineers (SPIE) Conference Series*
- Glendenning NK, ed. 2000. *Compact stars : nuclear physics, particle physics, and general relativity*
- Glendenning NK, Moszkowski SA. 1991. *Physical Review Letters* 67:2414–1417
- Glendenning NK, Schaffner-Bielich J. 1999. *Phys. Rev. C* 60:025803
- Goriely S, Chamel N, Pearson JM. 2010. *Phys. Rev. C* 82:035804
- Grindlay JE, Camilo F, Heinke CO, Edmonds PD, Cohn H, Lugger P. 2002. *ApJ* 581:470–484
- Guillot S, Rutledge RE. 2014. *ApJ* 796:L3
- Guillot S, Rutledge RE, Brown EF. 2011. *ApJ* 732:88
- Guillot S, Servillat M, Webb NA, Rutledge RE. 2013. *ApJ* 772:7
- Güver T, Özel F. 2013. *ApJ* 765:L1
- Güver T, Özel F, Cabrera-Lavers A, Wroblewski P. 2010a. *ApJ* 712:964–973
- Güver T, Özel F, Psaltis D. 2012. *ApJ* 747:77
- Güver T, Psaltis D, Özel F. 2012. *ApJ* 747:76
- Güver T, Wroblewski P, Camarota L, Özel F. 2010b. *ApJ* 719:1807–1812
- Haensel P, Zdunik JL, Schaefer R. 1986. *A&A* 160:121–128
- Harris WE. 1996. *AJ* 112:1487
- Harrison BK, Thorne KS, Wakano M, Wheeler JA. 1965. *Gravitation Theory and Gravitational Collapse*
- Hebel K, Lattimer JM, Pethick CJ, Schwenk A. 2010. *Physical Review Letters* 105:161102
- Heger A, Cumming A, Galloway DK, Woosley SE. 2007. *ApJ* 671:L141–L144
- Heinke CO, Cohn HN, Lugger PM, Webb NA, Ho WCG, et al. 2014. *MNRAS* 444:443–456
- Heinke CO, Rybicki GB, Narayan R, Grindlay JE. 2006. *ApJ* 644:1090–1103
- Hessels J, Possenti A, Bailes M, Bassa C, Freire PCC, et al. 2015. *Advancing Astrophysics with the Square Kilometre Array (AASKA14)* :47
- Hessels JWT, Ransom SM, Stairs IH, Freire PCC, Kaspi VM, Camilo F. 2006. *Science* 311:1901–1904
- Hewish A, Bell SJ, Pilkington JDH, Scott PF, Collins RA. 1968. *Nature* 217:709–713
- Hotokozaka K, Kyutoku K, Okawa H, Shibata M, Kiuchi K. 2011. *Phys. Rev. D* 83:124008
- Hulse RA, Taylor JH. 1975. *ApJ* 195:L51–L53
- Jacoby BA, Bailes M, van Kerkwijk MH, Ord S, Hotan A, et al. 2003. *ApJ* 599:L99–L102
- Jacoby BA, Cameron PB, Jenet FA, Anderson SB, Murty RN, Kulkarni SR. 2006. *ApJ* 644:L113–L116
- Jacoby BA, Hotan A, Bailes M, Ord S, Kulkarni SR. 2005. *ApJ* 629:L113–L116

- Janka HT, Langanke K, Marek A, Martínez-Pinedo G, Müller B. 2007. *Phys. Rep.* 442:38–74
- Janssen GH, Stappers BW, Kramer M, Nice DJ, Jessner A, et al. 2008. *A&A* 490:753–761
- Kajava JJE, Nättälä J, Latvala OM, Pursiainen M, Poutanen J, et al. 2014. *MNRAS* 445:4218–4234
- Kaplan DB, Nelson AE. 1986. *Physics Letters B* 175:57–63
- Kaplan DL, Boyles J, Dunlap BH, Tendulkar SP, Deller AT, et al. 2014a. *ApJ* 789:119
- Kaplan DL, van Kerkwijk MH, Koester D, Stairs IH, Ransom SM, et al. 2014b. *ApJ* 783:L23
- Kasian LE. 2012. *Radio observations of two binary pulsars*. Ph.D. thesis, The University of British Columbia
- Keith MJ, Jameson A, van Straten W, Bailes M, Johnston S, et al. 2010. *MNRAS* 409:619–627
- Keith MJ, Johnston S, Ray PS, Ferrara EC, Saz Parkinson PM, et al. 2011. *MNRAS* 414:1292–1300
- Kerr M, Camilo F, Johnson TJ, Ferrara EC, Guillemot L, et al. 2012. *ApJ* 748:L2
- Kiziltan B, Kottas A, De Yoreo M, Thorsett SE. 2013. *ApJ* 778:66
- Klüpfel P, Reinhard PG, Bürvenich TJ, Maruhn JA. 2009. *Phys. Rev. C* 79:034310
- Knispel B, Lyne AG, Stappers BW, Freire PCC, Lazarus P, et al. 2015. *ApJ* 806:140
- Kojo T, Powell PD, Song Y, Baym G. 2015. *Phys. Rev. D* 91:045003
- Kortelainen M, Lesinski T, Moré J, Nazarewicz W, Sarich J, et al. 2010. *Phys. Rev. C* 82:024313
- Kramer M, Stairs IH, Manchester RN, McLaughlin MA, Lyne AG, et al. 2006. *Science* 314:97–102
- Kramer M, Stappers B. 2015. *Advancing Astrophysics with the Square Kilometre Array (AASKA14)* :36
- Kumar P, Zhang B. 2015. *Phys. Rep.* 561:1–109
- Kurkela A, Fraga ES, Schaffner-Bielich J, Vuorinen A. 2014. *ApJ* 789:127
- Kuulkers E, den Hartog PR, in’t Zand JJM, Verbunt FWM, Harris WE, Cocchi M. 2003. *A&A* 399:663–680
- Lackey BD, Kyutoku K, Shibata M, Brady PR, Friedman JL. 2012. *Phys. Rev. D* 85:044061
- Lamb FK, Boutloukos S, Van Wassenhove S, Chamberlain RT, Lo KH, Miller MC. 2009. *ApJ* 705:L36–L39
- Lattimer JM. 2012. *Annual Review of Nuclear and Particle Science* 62:485–515
- Lattimer JM, Prakash M. 2001. *ApJ* 550:426–442
- Lattimer JM, Schutz BF. 2005. *ApJ* 629:979–984
- Lattimer JM, Steiner AW. 2014. *ApJ* 784:123
- Lazarus P. 2013. In *IAU Symposium*, ed. J van Leeuwen, vol. 291 of *IAU Symposium*
- Leahy DA, Morsink SM, Cadeau C. 2008. *ApJ* 672:1119–1126
- Leahy DA, Morsink SM, Chou Y. 2011. *ApJ* 742:17
- Leahy DA, Morsink SM, Chung YY, Chou Y. 2009. *ApJ* 691:1235–1242
- Lewin WHG, van Paradijs J, Taam RE. 1993. *Space Sci. Rev.* 62:223–389
- Lindblom L. 1992. *ApJ* 398:569–573
- Link B, Epstein RI, Lattimer JM. 1999. *Physical Review Letters* 83:3362–3365
- London RA, Taam RE, Howard WM. 1986. *ApJ* 306:170–182
- Lorimer DR. 2008. *Living Reviews in Relativity* 11:8
- Lynch RS, Boyles J, Ransom SM, Stairs IH, Lorimer DR, et al. 2013. *ApJ* 763:81
- Lynch tRS, Freire PCC, Ransom SM, Jacoby BA. 2012. *ApJ* 745:109
- Lyne AG, Burgay M, Kramer M, Possenti A, Manchester RN, et al. 2004. *Science* 303:1153–1157
- Madej J, Joss PC, Różańska A. 2004. *ApJ* 602:904–912
- Majczyna A, Madej J. 2005. *Acta Astron.* 55:349–366
- Majczyna A, Madej J, Joss PC, Różańska A. 2005. *A&A* 430:643–654
- Manchester RN, Hobbs GB, Teoh A, Hobbs M. 2005. *AJ* 129:1993–2006
- Manchester RN, Lyne AG, Camilo F, Bell JF, Kaspi VM, et al. 2001. *MNRAS* 328:17–35
- Martinez JG, Stovall K, Freire PCC, Deneva JS, Jenet FA, et al. 2015. *ApJ* In press
- Metzger BD, Martínez-Pinedo G, Darbha S, Quataert E, Arcones A, et al. 2010. *MNRAS* 406:2650–2662
- Miller MC, Lamb FK. 1998. *ApJ* 499:L37–L40
- Miller MC, Lamb FK, Psaltis D. 1998. *ApJ* 508:791–830
- Morales J, Pandharipande VR, Ravenhall DG. 2002. *Phys. Rev. C* 66:054308
- Morrison IA, Baumgarte TW, Shapiro SL, Pandharipande VR. 2004. *ApJ* 617:L135–L138
- Morsink SM, Leahy DA. 2011. *ApJ* 726:56
- Morsink SM, Leahy DA, Cadeau C, Braga J. 2007. *ApJ* 663:1244–1251
- Mukherjee A. 2009. *Phys. Rev. C* 79:045811

- Müller H, Serot BD. 1996. *Nuclear Physics A* 606:508–537
- Muno MP, Özel F, Chakrabarty D. 2002. *ApJ* 581:550–561
- Muno MP, Özel F, Chakrabarty D. 2003. *ApJ* 595:1066–1076
- Müther H, Prakash M, Ainsworth TL. 1987. *Physics Letters B* 199:469–474
- Nakar E. 2007. *Phys. Rep.* 442:166–236
- Nath NR, Strohmayer TE, Swank JH. 2002. *ApJ* 564:353–360
- Oppenheimer JR, Volkoff GM. 1939. *Physical Review* 55:374–381
- Orosz JA, Kuulkers E. 1999. *MNRAS* 305:132–142
- Özel F. 2001. *ApJ* 563:276–288
- Özel F. 2006. *Nature* 441:1115–1117
- Özel F. 2013. *Reports on Progress in Physics* 76:016901
- Özel F, Baym G, Güver T. 2010. *Phys. Rev. D* 82:101301
- Özel F, Gould A, Güver T. 2012. *ApJ* 748:5
- Özel F, Psaltis D. 2009. *Phys. Rev. D* 80:103003
- Özel F, Psaltis D, Güver T. 2015. *ArXiv e-prints*
- Özel F, Psaltis D, Güver T, Baym G, Heinke C, Guillot S. 2015. *ArXiv e-prints*
- Özel F, Psaltis D, Narayan R, Santos Villarreal A. 2012. *ApJ* 757:55
- Özel F, Psaltis D, Ransom S, Demorest P, Alford M. 2010. *ApJ* 724:L199–L202
- Paczynski B. 1983. *ApJ* 267:315–321
- Page D. 1995. *ApJ* 442:273–285
- Page D, Reddy S. 2006. *Annual Review of Nuclear and Particle Science* 56:327–374
- Pandharipande VR, Pethick CJ, Thorsson V. 1995. *Physical Review Letters* 75:4567–4570
- Pechenick KR, Ftaclas C, Cohen JM. 1983. *ApJ* 274:846–857
- Piekarewicz J, Agrawal BK, Colò G, Nazarewicz W, Paar N, et al. 2012. *Phys. Rev. C* 85:041302
- Portegies Zwart S, van den Heuvel EPJ, van Leeuwen J, Nelemans G. 2011. *ApJ* 734:55
- Potekhin AY, Fantina AF, Chamel N, Pearson JM, Goriely S. 2013. *A&A* 560:A48
- Poutanen J, Beloborodov AM. 2006. *MNRAS* 373:836–844
- Poutanen J, Gierliński M. 2003. *MNRAS* 343:1301–1311
- Poutanen J, Nättälä J, Kajava JJE, Latvala OM, Galloway DK, et al. 2014. *MNRAS* 442:3777–3790
- Prince TA, Anderson SB, Kulkarni SR, Wolszczan A. 1991. *ApJ* 374:L41–L44
- Psaltis D, Chakrabarty D. 1999. *ApJ* 521:332–340
- Psaltis D, Özel F. 2014. *ApJ* 792:87
- Psaltis D, Özel F, Chakrabarty D. 2014. *ApJ* 787:136
- Psaltis D, Özel F, DeDeo S. 2000. *ApJ* 544:390–396
- Ransom SM, Hessels JWT, Stairs IH, Freire PCC, Camilo F, et al. 2005. *Science* 307:892–896
- Ransom SM, Ray PS, Camilo F, Roberts MSE, Çelik Ö, et al. 2011. *ApJ* 727:L16
- Ransom SM, Stairs IH, Archibald AM, Hessels JWT, Kaplan DL, et al. 2014. *Nature* 505:520–524
- Rawls ML, Orosz JA, McClintock JE, Torres MAP, Bailyn CD, Buxton MM. 2011. *ApJ* 730:25
- Read JS, Baiotti L, Creighton JDE, Friedman JL, Giacomazzo B, et al. 2013. *Phys. Rev. D* 88:044042
- Read JS, Markakis C, Shibata M, Uryū K, Creighton JDE, Friedman JL. 2009. *Phys. Rev. D* 79:124033
- Reardon DJ, Hobbs G, Coles W, Levin Y, Keith MJ, et al. 2016. *MNRAS* 455:1751–1769
- Rikovska Stone J, Guichon PAM, Matevosyan HH, Thomas AW. 2007. *Nuclear Physics A* 792:341–369
- Roberts MSE, McLaughlin MA, Gentile PA, Ray PS, Ransom SM, Hessels JWT. 2015. *ArXiv e-prints*
- Roca-Maza X, Centelles M, Viñas X, Warda M. 2011. *Physical Review Letters* 106:252501
- Rutledge RE, Bildsten L, Brown EF, Pavlov GG, Zavlin VE. 2001. *ApJ* 551:921–928
- Ryba MF, Taylor JH. 1991. *ApJ* 371:739–748
- Schulze HJ, Lejeune A, Cugnon J, Baldo M, Lombardo U. 1995. *Physics Letters B* 355:21–26
- Splaver EM. 2004. *Long-term timing of millisecond pulsars*. Ph.D. thesis, PRINCETON UNIVERSITY
- Stairs IH. 2003. *Living Reviews in Relativity* 6:5
- Steiner AW, Lattimer JM, Brown EF. 2010. *ApJ* 722:33–54
- Steiner AW, Lattimer JM, Brown EF. 2013. *ApJ* 765:L5
- Stergioulas N, Friedman JL. 1995. *ApJ* 444:306–311

- Stovall K, et al. 2015. ApJ In preparation
- Stovall K, Lynch RS, Ransom SM, Archibald AM, Banaszak S, et al. 2014. ApJ 791:67
- Strohmayer TE, Zhang W, Swank JH. 1997. ApJ 487:L77–L80
- Strohmayer TE, Zhang W, Swank JH, Smale A, Titarchuk L, et al. 1996. ApJ 469:L9
- Suleimanov V, Poutanen J, Werner K. 2011. A&A 527:A139
- Suleimanov V, Poutanen J, Werner K. 2012. A&A 545:A120
- Swiggum JK, Rosen R, McLaughlin MA, Lorimer DR, Heatherly S, et al. 2015. ApJ 805:156
- Sztajno M, Fujimoto MY, van Paradijs J, Vacca WD, Lewin WHG, et al. 1987. MNRAS 226:39–55
- Tamii A, Poltoratska I, von Neumann-Cosel P, Fujita Y, Adachi T, et al. 2011. *Physical Review Letters* 107:062502
- Taylor JH, Fowler LA, McCulloch PM. 1979. Nature 277:437–440
- Thorsett SE, Chakrabarty D. 1999. ApJ 512:288–299
- Tolman RC. 1934. *Relativity, Thermodynamics, and Cosmology*
- Tolman RC. 1939. *Physical Review* 55:364–373
- Trippa L, Colò G, Vigezzi E. 2008. Phys. Rev. C 77:061304
- Tsang MB, Zhang Y, Danielewicz P, Famiano M, Li Z, et al. 2009. *Physical Review Letters* 102:122701
- van Kerkwijk MH, Breton RP, Kulkarni SR. 2011. ApJ 728:95
- van Kerkwijk MH, Kulkarni SR. 1999. ApJ 516:L25–L28
- van Leeuwen J, Kasian L, Stairs IH, Lorimer DR, Camilo F, et al. 2015. ApJ 798:118
- van Paradijs J. 1979. ApJ 234:609–611
- Verbiest JPW, Bailes M, van Straten W, Hobbs GB, Edwards RT, et al. 2008. ApJ 679:675–680
- Verbunt F, Freire PCC. 2014. A&A 561:A11
- Watts A, Andersson N, Chakrabarty D, Feroci M, Hebeler K, et al. 2015. *RMP* Submitted
- Watts AL. 2012. ARA&A 50:609–640
- Webb NA, Barret D. 2007. ApJ 671:727–733
- Weinberg N, Miller MC, Lamb DQ. 2001. ApJ 546:1098–1106
- Weisberg JM, Nice DJ, Taylor JH. 2010. ApJ 722:1030–1034
- Wex N. 2014. *ArXiv e-prints*
- Wheeler JA. 1966. ARA&A 4:393
- Witten E. 1984. Phys. Rev. D 30:272–285
- Yagi K, Stein LC, Pappas G, Yunes N, Apostolatos TA. 2014. Phys. Rev. D 90:063010
- Yagi K, Yunes N. 2013. Phys. Rev. D 88:023009
- Zamfir M, Cumming A, Galloway DK. 2012. ApJ 749:69
- Zavlin VE. 2006. ApJ 638:951–962
- Zavlin VE. 2007. Ap&SS 308:297–307
- Zavlin VE, Pavlov GG, Shibano Y. 1996. A&A 315:141–152
- Zhu WW, Stairs IH, Demorest PB, Nice DJ, Ellis JA, et al. 2015. ApJ 809:41